

AperTO - Archivio Istituzionale Open Access dell'Università di Torino

e l'onomastie du pastoralisme au
montagne et dans la culture de
la région alpine

This is a pre print version of the following article

Original Citation:

Availability:

This version is available <http://hdl.handle.net/2318/1757332> since 2020-10-19T18:36:55Z

Publisher:

Metis Presses

Terms of use:

Open Access

Anyone can freely access the full text of works made available as "Open Access". Works made available under a Creative Commons license can be used according to the terms and conditions of said license. Use of all other works requires consent of the right holder (author or publisher) if not exempted from copyright protection by the applicable law.

(Article begins on next page)

This is the author's final version of the contribution published as:

Ferrero S.; Bartoli O.; Cesare B.; Salvioli-Mariani E.; Acosta-Vigil A.; Cavallo A.; Groppo C.; Battiston S.. Microstructures of melt inclusions in anatectic metasedimentary rocks. *JOURNAL OF METAMORPHIC GEOLOGY*. 30 pp: 303-322.

DOI: 10.1111/j.1525-1314.2011.00968.x

The publisher's version is available at:

<http://doi.wiley.com/10.1111/j.1525-1314.2011.00968.x>

When citing, please refer to the published version.

Link to this full text:

<http://hdl.handle.net/2318/97172>

Microstructures of melt inclusions in anatectic metasedimentary rocks

Ferrero S.¹, Bartoli O.², Cesare B.¹, Salvioli Mariani E.², Cavallo A.³, Groppo C.⁴, Battiston S.⁵

¹*Dipartimento di Geoscienze, Università di Padova, via Giotto 1, 35137 Padova, Italy*

²*Dipartimento di Scienze della Terra, Università di Parma, Viale delle Scienze 78, 43100 Parma, Italy*

³*Istituto Nazionale di Geofisica e Vulcanologia (INGV), via di Vigna Murata 605, 00143 Roma, Italy*

⁴*Dipartimento di Scienze Mineralogiche e Petrologiche, Università di Torino, via Valperga Caluso 35, I-10125, Torino, Italy*

⁵*Istituto per l'energia e le interfasi (IENI), Corso Stati Uniti, 4, 35127 Padova, Italy*

Abstract

The recent finding of crystallized and glassy melt inclusions (MI) in high-grade, partially melted metapelites and metagraywackes opened up the possibility to investigate anatectic processes through the MI study technique. The present work expands the study of Cesare et al. (2009; 2011) by focussing on three case studies: Khondalites (India), Ronda migmatites (Spain) and Barun Gneiss (Nepal Himalaya). The results of a detailed microstructural investigation are here reported, along with some new microchemical data on MI bulk composition.

MI were trapped within peritectic garnet and ilmenite during their growth, and are therefore primary inclusions. Inclusions are generally isometric and very small in size, mostly $\leq 15 \mu\text{m}$, and only rarely $\leq 30 \mu\text{m}$. In most cases inclusions are crystallized (“nanogranites”), and contain a granitic phase assemblage with quartz, feldspars and one or two micas (depending on the case study), often along with accessory phases (mainly Zr, Ap, Rt). Besides nanogranites, partially crystallized inclusions are locally abundant, and also glassy inclusions, generally very small ($\leq 8 \mu\text{m}$) may occur in the same cluster. After entrapment, inclusions underwent limited microstructural modifications, such a diffuse shape maturation, locally necking-down processes, and decrepitation (mainly in Barun gneisses), which, however, did not influence their bulk composition. Re-homogenized nanogranites and glassy inclusions (where present) always show a leucogranitic and peraluminous melt, whose composition varies depending on the case study and it is generally consistent with the results of partial melting experiments on metapelites and metagraywackes.

27 Anatectic MI should therefore be considered as a new and important tool to understand the partial melting
28 processes, providing further constraints to anatectic melt composition in metasedimentary rocks.

29

30 **1) Introduction and aim of the study**

31 Melt inclusions (MI) represent a powerful tool to gain data on several processes of the Earth system, from
32 magma behavior during eruptions to the emplacement of plutons in the upper crust (Roedder, 1984; Student
33 & Bodnar, 1996; Webster, 2006). The abundance of MI in magmatic minerals was already recognized in the
34 XIX century by H.C. Sorby (1858), who published the first study of MI from various types of igneous rocks
35 (and also from some artificial products, such as slags), supported by a detailed petrological characterization.
36 Many of the considerations he made on this topic are still valid, e.g. the same approach and assumptions
37 applied to the interpretation of fluid inclusions (FI) in minerals may apply to MI (see also Roedder, 1984;
38 Bodnar & Student, 2006). Despite the long-lived interest in MI, a large amount of data became available only
39 with the spread of new in-situ microanalytical techniques. In particular, the development of electron
40 microprobes allowed the characterization of major and minor elements (e.g. Anderson, 1974; Melson, 1983),
41 while more recently trace elements can be quantified using laser ablation ICP-MS also (e.g. Halter et al.,
42 2002). Moreover, infrared spectroscopy, ion microprobe and new methods for analyses of hydrous glasses
43 make now possible to characterize and quantify also volatiles within the enclosed melt (see Sobolev, 1996
44 and related references). MI bulk composition determined by these means is likely to reflect magma chemistry
45 at depth (e.g. Roedder, 1979; Sobolev, 1996; Frezzotti, 2001).

46 Crystal phases that nucleate and grow in (or along with) a magma have the chance of enclosing portions of
47 the melt present at the moment of their growth (Roedder, 1984). When metamorphic rocks undergo partial
48 melting with incongruent reactions, droplets of melt may be trapped as inclusions by the peritectic phase(s)
49 that is nucleating at the same time the melt is produced (Cesare, 2008). Petrologists' chance to study those
50 small portions of trapped melt mainly resides on their preservation during their retrograde path.
51 Unfortunately, between the partial melting and the exhumation on the Earth's surface, high-grade

52 metamorphic rocks generally reside for a long time at P-T conditions likely to produce changes in the
53 peritectic phases, e.g. retrograde reactions, re-crystallization, with subsequent erasure and/or modifications of
54 the MI possibly present.

55 Although it is intuitive that peritectic phases may trap anatectic MI, no clear and natural evidence was
56 reported until the finding of primary glassy MI in metapelitic enclaves (Cesare et al., 1997) from the
57 Neogene Volcanic Province (NVP), Spain. These MI did not undergo the effects of a slow cooling, because
58 the enclaves were rapidly brought up to the surface. This case of frozen “migmatites-in-progress” preserved
59 many of the features they had at depth, allowing the verification of many of the current ideas on the
60 mechanisms of partial melting, derived by the petrological characterization of classic migmatites (Cesare,
61 2008 and references therein). Glassy inclusions from the NVP are believed to contain the anatectic melt
62 produced during the prograde path of the rock at $T > 700\text{ }^{\circ}\text{C}$ and preserved by rapid cooling, as confirmed by
63 microstructural and compositional characterization (see Cesare et al., 2007; Ferrero et al., 2010 for major
64 elements; see Acosta-Vigil et al., 2007, 2010 for major and trace elements). Proof of the occurrence of
65 anatectic MI also in classic migmatitic terrains came with the finding of mainly crystallized MI within
66 Khondalites from Kerala Khondalite Belt (KKB, India), reported by Cesare et al., (2009). These MI occur in
67 peritectic garnets, and show a bulk composition consistent with that expected from the partial melting of
68 metapelites at T approaching 900°C . The generally granitic phase assemblage, the sub- μm grain size often
69 observed and the presence of igneous microstructures led to the choice of the name “nanogranites” (Cesare et
70 al., 2009) for these inclusions.

71 The reported case studies demonstrate that it is possible to apply the MI study techniques to the
72 characterization of anatectic processes in migmatites and granulites, a fundamental point in the understanding
73 of the crustal differentiation through time (Brown & Rushmer, 2006). The composition of the anatectic melt is
74 commonly investigated by focusing on migmatites, in particular on the leucosome produced by the
75 crystallization of the anatectic melt. However, several processes, such as cumulus phenomena, entrainment of
76 xenocrysts and fractional crystallization, may change its composition. This fact makes any estimation based

77 on the chemical composition of leucosomes highly questionable (Sawyer, 1996, 2008; Marchildon and
78 Brown, 2001). To overcome the problems listed above, the experimental approach became in the last decades
79 a well established tool in partial melting investigation on metapelites and metagraywackes (e.g., Thompson
80 1982; Vielzeuf & Holloway 1988; Carrington & Harley 1995; Gardien et al. 1995; Stevens et al. 1997;
81 Patiño-Douce & Harris 1998), since they are the most fertile (melt-producing) lithologies in the middle crust.
82 However, also in this case it must be considered that experimental conditions cannot entirely reproduce those
83 at which partial melting takes place in nature, in terms of both a_{H_2O} and bulk rock composition.

84 The finding of anatectic MI in migmatites gives us now the chance to study anatectic melt *in situ* within
85 natural samples. In this case, the real challenge becomes the small size of the anatectic MI. Inclusions in
86 KKB are $\leq 30 \mu\text{m}$ in diameter, and contain an aggregate of quartz, biotite, K-feldspar and plagioclase, close
87 or beyond the resolution limits of many analytical instruments. Cesare et al. (2009) showed that these MI can
88 be thoroughly characterized by using high resolution electron microscopes and microprobes. Not
89 surprisingly, these inclusions strongly resemble the sketches of Sorby (1858) of MI, author's "stone cavities",
90 in plutonic rocks, although Sorby's inclusions are generally larger. Both anatectic and plutonic MI are
91 partially/totally crystallized (or devitrified) (Frezzotti et al., 1992), as expected for melt droplets in slowly
92 cooled rocks, and are small in size, see e.g. MI in Erzgebirge granites which show mean diameter $10 \mu\text{m}$
93 (Thomas et al., 1996).

94 The two case studies previously reported, MI in Spanish enclaves and in Khondalites, represent the first
95 detailed characterization with modern high-resolution techniques. Two previous cases of MI in migmatitic
96 rocks are briefly reported in literature. Tomilenko and Chupin (1983; see also Touret and Olsen, 1985)
97 discuss small ($\leq 10 \mu\text{m}$ across) silicate inclusions in high grade terrains, containing an unknown silicate phase
98 along with crystals, and often a shrinkage bubble. However, since they occur in quartz and plagioclase within
99 the leucosome, these MI probably did not form during prograde melting, and therefore do not contain the
100 original anatectic melt produced during the prograde history of the rock. In the second case, Hartel et al.
101 (1990) reports crystallized MI in garnet from felsic migmatites collected in the western central Sulawesi,

102 Indonesia. They are commonly crystallized MI, 2-10 μm across, with dodecahedral shape and a roughly
103 granitic composition -from microchemical data obtained by using a defocalized analytical beam and
104 subtracting the estimated host contribution. Such inclusions were interpreted as containing melt produced by
105 biotite dehydration melting, although compositional data are limited due to the MI average size.

106 This study aims to present and discuss anatectic MI features in greater detail with respect to the previous
107 works of Cesare et al. (2009; 2011). With reference to three different case studies of migmatitic-granulitic
108 terrains, Khondalites (KKB, India), Ronda migmatites (Betic Cordilleras, SE Spain) and Barun Gneiss
109 (Higher Himalayan Crystalline or HCC, Nepal), the emphasis of this paper is primarily microstructural. The
110 chosen case studies are high-grade metasedimentary rocks which experienced different P-T evolutions. New
111 microstructural and microchemical data on anatectic MI in Khondalites and in Ronda migmatites are
112 presented and discussed in this paper, along with a detailed study of MI in Barun gneisses, firstly reported by
113 Groppo et al., (submitted). The characterization of the host minerals, the MI microstructures and the internal
114 crystallization microstructures of the phases was performed by using both optical and FEG microscopes. The
115 bulk composition of the trapped phase was then investigated by re-melting crystallized inclusions and
116 analyzing them with an electron microprobe using a very narrow electron beam.

117 The three selected case studies are the first studied from a continuously-growing list of findings from
118 different geological settings, including Ivrea-Verbano Zone (T.Ewing, Pers. Comm.), Adirondacks
119 mountains (Henriquez & Darling, 2009), Massachusettes (J.Thomson. Pers. Comm.), Argentera Massif
120 (Ferrero), Ulten zone (Braga & Massonne, 2008) and La Galite archipelago (R. Braga, Pers. Comm.). Many
121 of the listed case studies are within intensively studied terrains, where anatectic MI have been evidently
122 overlooked until now. Moreover, the length of the case study list by itself suggests that anatectic MI are less
123 rare than what expected and may then be present in many high-grade terrains, in spite of the fact that they
124 were (almost) never reported in literature until now.

126 **2) Geological setting and petrography**

127 The first case study consists of garnet-sillimanite-graphite gneisses, named khondalites, from KKB in
128 southern India, that underwent anatexis at HT/UHT conditions during the PanAfrican event (Chacko et al.,
129 1996). At the outcrop scale these rocks are stromatic diatexites, coarse to medium in grain size (Fig. 1a). The
130 melanosome consists of large garnet and cordierite porphyroblasts, ≤ 2 cm across, coarse-grained sillimanite,
131 biotite, ilmenite, green spinel and a small amounts of feldspar, along with flakes of graphite. The leucosome
132 consists of quartz and massive feldspar porphyroblasts, up to 5 mm, and locally plagioclase is abundant.
133 Melanosome may be distinguished in Bt-poor and Bt-rich types even at thin section scale, possibly reflecting
134 a non homogeneous protolith with a more or less refractory assemblage. The Bt-rich melanosome shows a
135 spaced foliation, due to iso-orientation of coarse-grained sillimanite and biotite, while the Bt-poor
136 melanosome is not internally foliated, but defines a mineralogical banding through interfingering with
137 leucosome domains. These migmatites experienced a counter-clockwise PT evolution, with a partial melting
138 event, corresponding to the metamorphic peak, around 900°C (Braun et al., 1996; Shabeer et al., 2005,) and
139 0.6-0.8 GPa (Cenki et al., 2002), followed by an almost isobaric cooling down to 800°C (Nandakumar &
140 Harley, 2000) and then an isothermal decompression to 0.55 – 0.3 GPa (Santosh, 1986; Chacko et al., 1987).

141 Ronda migmatites are located at the western part of the Internal Zone of the Betic Cordillera (SE Spain)
142 and underlie the Ronda peridotites. The migmatites range from metatexites (Fig. 1b), diatexites to mylonitic
143 migmatites towards the contact with the overlying peridotites (Acosta-Vigil et al., 2001; Esteban et al.,
144 2008). The hot thrusting of the peridotites over a metasedimentary sequence produced a dynamothermal
145 aureole during the Alpine Orogeny (Tubía & Cuevas, 1986; Tubía et al., 1997; Platt & Whitehouse, 1999).
146 However, SHRIMP studies on zircons (Sánchez-Rodríguez, 1998; Acosta-Vigil, in preparation) have yielded
147 both Hercynian and Alpine ages, suggesting the existence of two different anatectic events separated in time.
148 The peridotite overthrusting and HT metamorphism occurred during decompression in a syn-collisional
149 tectonic setting (Tubía et al., 1997; Platt et al., 2003). The outcrops consist of stromatic metatexite, nebulitic
150 or deformed diatexites and mylonitic migmatites; the melanocratic portion contains garnet, biotite,
151 sillimanite, graphite, ilmenite, plagioclase and quartz. Leucosomes in metatexites and mylonites consist of

152 quartz, plagioclase, K-feldspar and rare biotite and garnet. Ronda migmatites underwent a partial melting
153 event at 700-800 °C and 0.5-0.8 GPa (Torres-Roldán, 1983; Tubía & Cuevas, 1986; Tubía et al., 1997); the
154 temperature and pressure of metamorphic peak increase from metatexites to mylonitic migmatites. The T
155 peak was followed by rapid cooling (400-200 °C/Ma, Platt et al. 2003; Esteban et al. 2004).

156 Barun Gneiss (Bordet, 1961) occur at the base of the HHC at the higher structural levels of the Himalayan
157 belt, in Eastern Nepal. This granulitic/migmatitic belt, which extends toward the east in Sikkim and Bhutan
158 (e.g. Goscombe et al., 2006 and references therein) underwent high grade metamorphism and partial melting
159 during the Alpine-Himalayan orogeny (28-16 Ma, Viskupic & Hodges, 2001). At the outcrop scale Barun
160 gneisses present a discontinuous planar foliation, defined by mm-thick layers of melanosomes alternating
161 with elongated leucosome domains, up to 1 cm in thickness. Two different samples, 07-19 and 07-36, were
162 investigated in this work, both of them with mineralogical and microstructural features very close to those of
163 sample 07-35 studied in detail by Groppo et al. (submitted). The fine-grained melanosome consists of small-
164 sized biotite, sillimanite and plagioclase plus quartz, with locally abundant garnet porphyroblasts, ≤ 5 mm
165 across, wrapped by the foliation. Garnet occurs both as subhedral poikiloblasts (sample 07-36) and skeletal
166 porphyroblasts (sample 07-19). Kyanite may also occur as a relic, rimmed by a thick plagioclase corona.
167 Leucosome levels consist of quartz, K-feldspar and plagioclase. Based on the petrogenetic modeling, Barun
168 gneisses underwent a clockwise PT path, with nearly isobaric heating up to 800-860°C at 0.8 GPa with
169 partial melting, followed by a near isothermal decompression down to 0.65 GPa, when the crystallization of
170 the melt is believed to have taken place, and by a slightly decompressional cooling along a less steep
171 retrograde path (Groppo et al., submitted).

172 The presence of melt in the investigated rocks may be inferred based on the occurrence of several
173 microstructural evidences. Besides the presence of leucosome domains (Fig. 1c), pseudomorphs of melt-
174 filled pores (Holness and Sawyer, 2008) commonly occur. They mainly consist of quartz and plagioclase that
175 crystallize as grains with a cusped-lobate shape, mimicking the original geometry of the pore they were
176 confined in, often at the contact between MI-bearing garnet porphyroblasts and leucosome domains (Fig. 1c-

177 h). In Barun gneisses melt pseudomorphs commonly occur within large polymineralic inclusions of
178 Qtz+Pl+Bt in garnet, described in detail by Groppo et al. (submitted). They usually consist of films and shells
179 of plagioclase surrounding rounded quartz or biotite, with locally biotite growing from inclusion walls
180 toward the inner part of the volume. Similar features suggest those aggregates were originally large pockets
181 of melt, ≤ 300 μm wide. However, such a large size is likely to favour the entrapment of crystal phases
182 already present in the rock, and moreover they are never fully enclosed in the garnet. Their composition is
183 therefore modally unconstrained, not allowing estimation of the melt bulk chemistry. Further witnesses to the
184 former presence of melt are symplectites (Vernon, 2011), due to garnet retrograde reaction with the melt, e.g.
185 the quartz-cordierite symplectites often observed in khondalites or the biotite+plagioclase symplectites in the
186 Barun gneisses.

187 Although some of the microstructures reported above represent reliable indications for the former presence
188 of melt in the investigated rocks, none of them allows for the composition of the anatectic melt to be
189 retrieved. This target was accomplished below, using the novel approach based on MI.

191 **3) Methods**

192 The study of anatectic MI has been performed on about 50 thin and doubly-polished thick sections. The
193 thickness of the doubly-polished sections is variable and ranges 100-250 μm depending on the samples. In
194 some cases, garnets were separated from crushed thick sections. The characterization of the MI features,
195 phase assemblage and crystallization microstructures was carried out using different instrumental devices.
196 Petrographic characterization was carried out with optical microscope both in transmitted and reflected light,
197 in order to verify the occurrence of MI also in opaque minerals, i.e. Fe and Ti oxides. Crystallized minerals
198 and chemistry of the components were investigated by secondary electrons (SE) and back-scattered electrons
199 (BSE) imaging, semi-quantitative energy dispersive X-ray spectroscopy (EDS) analyses and X-ray mapping.
200 Data were collected with different scanning electron microscopes (SEM): 1) a CAM SCAN MX2500,
201 equipped with LaB6 cathod, at the Department of Geosciences, University of Padova; 2) a Jeol JSM-6500F

202 thermal Field Emission Scanning Electron Microscope (FESEM), available at the High Temperature/High
203 Pressure Laboratory, I.N.G.V. (Istituto Nazionale Geofisica e Vulcanologia), Rome; 3) a FEI Quanta 600
204 FEG, equipped with a Bruker EDX-Silicon Drifted Detector, available at the Nanoscale Characterization and
205 Fabrication Laboratory, I.C.T.A.S. (Institute for Critical Technology and Applied Science), Virginia Tech,
206 USA; 4) a SEM Zeiss equipped with FEG Gemini and a Silicon Drifted detector at CNR-IENI, Padova. BSE
207 images were acquired at variable magnifications and variable accelerating voltages, commonly 8 to 15 kV
208 depending on the used machine. Elemental X-ray maps were acquired at 20 and 15kV accelerating voltage
209 and at variable magnifications, in the range 5000-6000X, depending on the MI size, with resolution of
210 500X375 pixel.

211 MI re-homogenization was obtained with different techniques. A LINKAM TS1500 high temperature and
212 ambient pressure stage, in an inert atmosphere of He to prevent sample oxidation, was used to re-melt
213 anatectic MI in khondalites and Barun gneisses at the Fluid Inclusion Laboratory, Earth Science Department-
214 University of Parma, Italy. Inclusions were re-homogenized within doubly polished chips of garnet. A
215 temperature correction factor was applied, after having determined a calibration curve with different
216 standards of $K_2Cr_2O_7$, Ag and Au with melting T respectively of 398°C, 962°C and 1064°C. The accuracy of
217 measurements is $\pm 15^\circ$. KKB samples were heated up to 500°C with a rate of 50°C/min, followed by a 2
218 hours stop. Then MI were heated at 40°C/min up to the beginning of melting, i.e. when crystallized
219 inclusions under observation showed some modifications of the internal crystal boundaries. The samples
220 were then kept at this T for 15-30 min to allow a complete homogenization, and quenched afterwards in
221 liquid nitrogen to avoid as much as possible glass re-crystallization. Homogenization T values obtained
222 through this approach is $\sim 1040^\circ C$. A different ramp was selected for Barun samples, since the ramp of KKB
223 samples caused diffuse MI decrepitation. After being heated up to $\sim 550^\circ C$, the sample was brought to
224 $\sim 750^\circ C$, with stops of 10 min every 100°C, and up to 830°C (observed melting T) with 5 min stops every
225 25°C. The heating rate applied during the entire experiment is 50°C/min. Homogenized MI were then
226 selected by optical microscope investigation, and exposed to the surface through a careful polishing process,

227 where possible done by hand on abrasive sheets coated of Al₂O₃ and SiC with variable grain-size, to impose
228 less stress to the sample surface. MI in Ronda migmatites were re-homogenized at high pressure with a
229 piston cylinder apparatus at Laboratorio di Petrologia Sperimentale, Dipartimento di Scienze della Terra,
230 Università di Milano. The experimental conditions were 700 °C, 0.5 GPa and 24 h.

231 The MI microchemical composition was determined both in glassy inclusions and in homogenized
232 inclusions using two different Jeol JXA 8200 Superprobes at the High Temperature/High Pressure
233 Laboratory, I.N.G.V., Rome, and at the Dipartimento di Scienze della Terra, Università di Milano. Used
234 analytical conditions were selected depending on the machine and the case study, always using a 15 kV
235 accelerating voltage and a focused beam with size of 1 μm. Analytical parameters (beam current and
236 acquisition time) vary as follow: 1) in Ronda migmatites, 2 nA and 10 s on the peak and 5 on background; 2)
237 in Barun samples 6 nA, 5 s on peak and 2 on the background; 3) in KKB samples 3.5 nA and 10 s on peak
238 and 5 on background.

239 Na is known to migrate out of the electron beam excitation volume, and this may render the EMP data
240 unrepresentative of the analyzed melt. Therefore, according to Morgan & London (2005), correction factors
241 for Na, Si, Al and K were calculated from the ratio between analyzed and known concentrations of the
242 correspondent oxides within different glass standards, selected to be as close as possible in composition to
243 each of the analysed sample (in particular as H₂O contents). The used standards are respectively a 10 wt%
244 H₂O bearing glass (LGB 5; Behrens & Jantos, 2001), a 6.6 wt% H₂O-bearing melt (Morgan & London,
245 2005) and a 5.5 wt% H₂O glass from Acosta-Vigil et al. (2003). The Na loss was estimated as 23% relative
246 for Ronda migmatites, 8% in Barun samples and none in khondalites. Hand-by-hand selection of analytical
247 points allowed to verify the real position of the analytical beam, avoiding instrumental drift.

249 **4) Microstructural and chemical characterization of anatectic melt inclusions**

250 **4.1) Occurrence and optical features**

251 Anatectic MI have been recognized, so far, mainly within garnet in the three investigated cases (Fig. 2a,f),
252 although they locally occur also in ilmenite in metatexites from Ronda (Fig. 3).

253 MI-bearing garnets have different features and size. In khondalites, garnets form large anhedral
254 porphyroblasts (≤ 2 cm wide) located in the melanocratic portion of the diatexite, often not in touch with
255 leucosome because sheltered by cordierite overgrowths. The garnet in the leucosome are always MI-free. In
256 metatexites from Ronda, garnet crystals are generally subhedral and small (≤ 200 μm across; fig. 2b,e),
257 surrounded by leucosome that may form melt pseudomorph microstructures around garnets (Fig. 1e,f). In
258 more foliated samples, e.g. mylonites at the contact with Ronda peridotites, MI-bearing garnets are more
259 rare. The rare MI-bearing ilmenites occur as anhedral crystals (100-200 μm across) in the rock matrix (Fig.
260 3). In Barun gneisses MI occur both in poikiloblastic and skeletal garnets, ≤ 1 cm across (Fig. 2c,f).

261 The abundance and the microstructural distribution of MI in garnet vary depending on the case study. In
262 Barun gneisses MI are less abundant than in the other two cases, and show no preferred microstructural
263 position in skeletal garnets, while they mainly occur at the periphery of the crystal in poikiloblastic garnets,
264 where mineral inclusions and polymineralic inclusions are absent. Locally MI are clustered, forming groups
265 of tens of inclusions, often characterized by similar size. Where garnet is relatively mineral inclusion-free, as
266 in khondalites and Ronda migmatites, MI may form clusters of tens to hundreds of inclusions, locally with a
267 spherical geometry. Clusters do not have preferential location in anhedral porphyroblasts, such as in KKB
268 samples (Fig. 2a,d) while in subhedral to euhedral hosts, i.e. in Ronda metatexites, they occur at the core
269 (Fig. 2b,e), leaving a more or less narrow MI-free rim (similarly to what reported in garnets from El Hoyazo
270 enclaves, Acosta-Vigil et al., 2007). In ilmenite MI occur both as isolated and grouped inclusions with no
271 preferred microstructural position (Fig. 3). Locally the MI cluster may touch the host boundary, if the crystal
272 has been partially replaced by some retrograde mineral, e.g. biotite on garnet as in Ronda migmatites. No
273 proofs of secondary entrapment, such as linear arrays of MI, were observed.

274 The observed spatial arrangement as cluster is a strong constraint to the primary nature of MI with respect
275 to the host crystal (Roedder, 1984), i.e. they were trapped when garnet was growing. Both in KKB and

276 Ronda samples MI are evenly distributed within the clusters. However, if the average mutual distances
277 among adjacent MI are evaluated, they show a different “degree of packing” with the average varying from
278 $\leq 15 \mu\text{m}$ in Ronda samples to 80-100 μm in the khondalites (Fig. 2d,e).

279 Within clusters, mineral inclusions of size comparable to MI, i.e. $\leq 15 \mu\text{m}$, often occur. They mainly
280 consist of accessory minerals: apatite, rutile, zircon are widespread, while spinel occurs only in khondalites.
281 Depending on the case study also quartz, plagioclase, rarely graphite and fibrolite needles may be present. As
282 already observed in El Hoyazo enclaves by Acosta-Vigil et al. (2007), MI generally do not occur in the
283 surroundings of large mineral inclusions ($> 50 \mu\text{m}$), e.g. in Barun samples the mineral inclusion-rich core is
284 poor in MI with respect to the rim. Similar occurrence is visible in poikiloblastic garnet in khondalites, which
285 coexist at the thin section scale with MI-bearing garnets, completely free of mineral inclusions.

286 Investigated inclusions appear as small dots that might be misinterpreted at a first glance as defects of the
287 polished surface, in the case of very small ($< 10 \mu\text{m}$) inclusions. However a careful microscope investigation
288 shows that they are three-dimensional objects confined within the thin-section (fig. 2d-f). Two different types
289 of inclusions may be distinguished at optical investigation. The first type consists of dark-brownish
290 inclusions, containing a polymineralic aggregate as confirmed by the presence of different birefringent
291 crystals at crossed polars (Fig. 4a,b,e,f,i,l). This inclusion type represents the majority of the reported MI in
292 the investigated case studies, e.g. 85% in khondalites (Cesare et al., 2009). The second type of inclusions is
293 partially transparent in transmitted light and isotropic at crossed polars, always with a single birefringent
294 mineral (Fig. 4c,d,g,h). Raman spectroscopy, SEM and EMP investigations (Cesare et al., 2009, 2011)
295 showed that this inclusion type contain glass along with one or more accessory phases. Glassy inclusions in
296 Ronda metatexites are more rare than in KKB samples, and totally absent in Barun samples.

297 The shape is isometric in both inclusion types (Figg. 2;3;4;5) and the average size is $\leq 50 \mu\text{m}$. As general
298 observation, smallest (as average size) inclusions occur in Ronda garnets, $\sim 5 \mu\text{m}$, while they are slightly
299 larger ($\sim 15 \mu\text{m}$) in khondalites, where the MI size population define a Gaussian distribution (Cesare et al.,
300 2009). MI size in Ronda ilmenites ranges from 1.5 to 20 μm . In Barun gneisses MI range from few μm up to

301 50 μm , and only the smallest ones, with average size $\sim 8\text{-}10\ \mu\text{m}$, show a regular isometric shape, while larger
302 MI have an irregular shape and are characterized by the presence of offshoots, containing birefringent
303 minerals. The last MI type represents the most part of the MI observed in these samples. Their offshoots are
304 generally many times in length the MI diameter, with irregular distribution around the MI. Locally they may
305 connect two or more inclusions if close to each other (Fig. 4m,n). Similar features, although less common,
306 are also observed in khondalites MI, where some inclusions have one or two “tails” roughly opposite in
307 orientation and shorter in length, usually \leq MI diameter, with respect to Barun Gneiss samples (Fig. 4g).
308 Besides isometric and highly-irregular inclusions, locally tubular inclusions are observed (Fig. 2c,d), more
309 abundant in Barun gneisses. In few cases polycrystalline inclusions are acicular with diameter $\sim 5\text{-}6\ \mu\text{m}$ and
310 length $\leq 100\ \mu\text{m}$, where melt adhered to elongated phases, such as rutile needles.

312 **4.2) Microstructures and phase assemblage**

313 The isometric shape, visible under optical microscope observation, corresponds to a more or less
314 developed negative-crystal shape when MI are investigated at the FESEM (Fig. 5; see also Cesare et al.,
315 2011). This shape is generally developed in smallest inclusions, i.e. $\leq 20\ \mu\text{m}$ (Fig. 5a,b,e,h), unless the
316 presence of accessory minerals touching the MI walls (Fig. 5d). Larger inclusions are more irregular,
317 although they commonly have planar boundaries.

318 Within polycrystalline inclusions, the FESEM investigation shows different phase assemblages in different
319 case studies. Both crystallized inclusions in Barun (Fig. 5b,c;6a) and Ronda garnets (Fig. 5d,e) may contain
320 quartz, plagioclase, biotite and muscovite, and in the latter case study also minor K-feldspar may occur,
321 while within ilmenites crystallized inclusions contain quartz, biotite and plagioclase. Various accessory
322 minerals are commonly present: in particular, rutile is abundant in mylonitic migmatites at Ronda (Fig. 5d),
323 while zircon is more common in Himalayan samples. In khondalites instead MI do not contain muscovite,
324 and the phase assemblage consists of quartz, K-feldspar and biotite, with minor Na-rich plagioclase (Fig.
325 5a,f). Apatite and spinel are the most common accessories.

326 Generally the largest grains within crystallized inclusions consist of subhedral to euhedral grains of micas,
327 $\leq 5 \mu\text{m}$ in size (Fig. 5b,c), and they are likely to be the first phases to have crystallized. Locally muscovite
328 grows in continuity with biotite (Fig. 5c;6a). Both phases are often easily distinguishable in SE and BSE
329 images because of the basal cleavage and the irregular surface, due to the polishing process (Fig. 5f).
330 Usually K-feldspar and plagioclase form subhedral to anhedral crystals after Bt and/or Ms growth, with size
331 variable from hundreds of nanometers up to few microns, depending on the inclusion, while quartz often
332 occurs as interstitial phase. Igneous microstructures, such as granophyric intergrowths, are widespread
333 especially in khondalites and Barun Gneiss samples. In the first case study, quartz may form angular-wedge
334 like shape crystals (“micrographic” shape) crystallizing along with K-feldspar (Fig. 6b). Locally K-feldspar,
335 associated with biotite, occurs as worm-like grains embedded in large quartz grains (Fig. 5f). Quartz may
336 crystallize as cuneiform rods along with plagioclase in Barun samples (Fig. 5c). Elongated quartz rods are
337 moreover visible within plagioclase in khondalites (Fig. 11a in Cesare et al., 2011). Pseudomorphs of melt
338 filled pores, reported at the thin section scale, occur also inside the MI, at the tens-of-nanometers scale
339 (Cesare et al. 2009; 2011). The same accessory phases visible along MI in clusters occur also inside the
340 inclusions, often indented into the host mineral (Fig. 4h). Some MI show a diffuse nanoporosity, due to the
341 higher density of the crystallized phases with respect to the original melt. At Ronda, this nanoporosity is
342 filled with H_2O (M.L.Frezzotti, Pers. Comm.), suggesting a hydrous melt as confirmed by microchemical
343 data (see below).

344 Investigated MI show however a variable degree of crystallization, from total (nanogranites) to none
345 (glassy inclusions). Fully glassy inclusions contain an homogeneous glass, and occurs along with the same
346 accessory phases found in nanogranites (Fig. 5h). Their shape is often a negative crystal shape, more
347 developed in khondalites samples with respect to the Ronda ones.

348 The abundance of partially crystallized inclusions is variable. While they represent the largest portion of
349 MI in Ronda migmatites, in KKB and Barun Gneiss samples most MI consist of nanogranites. Partially
350 crystallized inclusion are indistinguishable from nanogranites at the optical microscope because of the small

351 size: the presence of a residual melt along with crystal phases is revealed by FESEM investigation and
352 elemental mapping. This amorphous phase may occupy different percentages of MI area, i.e. 20 to 60% in
353 khondalites. Residual melt is generally characterized by a diffuse nanoporosity, mainly localized at the
354 interface melt/crystal phases (Fig. 5g), and occurs along with a set of mineral phases quite constant in each
355 case study. One or two micas are often present, supporting the inference they are the first phases to
356 crystallize. In detail, in khondalites residual melt occurs along with Bt+Kfs+Qtz (Fig. 5g), while in Barun
357 migmatites the melt-coexistent assemblage is Bt+Ms+Pl+Qtz. In Ronda samples partially crystallized
358 inclusions generally contain Ms+Bt+Qtz along with residual melt, although, more rarely, Na-rich plagioclase
359 may be the only crystal phase present along with residual melt. The melt presence has been also confirmed
360 by the EMP analyses and the elemental maps collected both on nanogranites and on partially crystallized MI.
361 If compared, elemental distributions are different between the two different inclusion types. In Khondalites
362 Na, Ca and Cl are mainly partitioned in the residual melt (Fig. 7), while in melt absence, i.e. within
363 nanogranites, the same elements show the highest concentration respectively in plagioclase, apatite and
364 biotite. Similarly, in Barun samples the residual melt is characterized by the highest concentration of Na and
365 Ca, and minor amount of K, preferentially partitioned in micas. Often the residual melt shows cusped-lobate
366 geometries, like films surrounding some minerals (Fig. 7), resembling the pseudomorphs of melt-filled pores
367 observed at larger scale in the investigated rocks. These microstructures may be actually regarded as the
368 natural precursors of the melt pseudomorphs, since they still contain glass instead of crystallized phases.

369 Irregularly shaped MI in Barun gneisses present offshoots filled with biotite and quartz (Fig. 8b), while in
370 Khondalites only biotite crystallize in them (Fig. 5g,h). Generally their length is \leq MI radius in KKB
371 samples, and \gg MI radius in Barun Gneiss samples. In case of developed negative crystal shape, offshoots
372 usually occur at the corners of the inclusions outward, locally defining a radial arrangement (Fig. 8a). Along
373 with negative crystal shaped and irregular inclusions, in Barun samples necking down phenomena are visible,
374 such as fully crystallized inclusions with hourglass shape, interpreted as a former elongate inclusion that
375 underwent an incomplete separation in two different volumes of melt, now both crystallized (Fig. 8b).

376

377 **4.3) Microthermometry on nanogranites**

378 The large variability in microstructures and grain size within nanogranites, coupled with their small
379 diameters, does not allow a reliable estimate of their modal composition based on image analysis. Only
380 glassy inclusions may be analyzed directly by EMP means, but they are rare (or absent, e.g. in Barun
381 samples), and with size often below analytical limits. Re-heating experiments have been then performed to
382 re-melt nanogranites, restoring their original homogeneity and allowing to perform EMP analyses on the
383 enclosed melt (Lowenstern, 2003).

384 After re-melting experiments it has been observed that only MI in Ronda migmatites, reheated at high
385 pressure by using a piston cylinder apparatus, reached a complete, melt + vapor homogenization (Fig. 9a),
386 commonly observed in re-homogenization experiments performed on igneous MI. Experiments on KKB and
387 Barun samples were instead performed at ambient P conditions with high-temperature stage, and the re-
388 melted nanogranites always contain one or more bubbles along with a homogeneous melt (Fig. 9b). After
389 experimental runs, the MI population in re-heated samples consists of fully re-homogenized inclusions and
390 partially re-melted inclusions, containing still relics of the original phase assemblage and characterized by the
391 occurrence of decrepitation cracks. Generally larger nanogranites in each samples did not undergo
392 homogenization, and after re-heating they appear darker and often with microcracks.

393 Our investigation focused on the first type of inclusions, after a careful selection performed via optical and
394 electron microscope to verify the homogeneity of the melt under analysis. Homogenized inclusions maintain
395 both the isometric shape, locally also negative-crystal, and solid inclusions observed in original nanogranites,
396 i.e. accessory minerals. In samples re-heated with heating stage, $\leq 10 \mu\text{m}$ long cracks, filled with melt, are
397 often visible also in fully homogenized inclusions. In khondalites and Barun gneisses these cracks are often
398 dark at optical observation, due to the precipitation of cubic Fe-oxides grains. The same mineral phase may
399 occur also in limited embayments on the MI walls. Locally, a crystal phase similar in composition to a high-
400 T orthopyroxene (e.g. Sato, 2004) occur in the KKB samples, likely to be considered a product of garnet-melt

401 interaction due to overheating during HT experiments. Decrepitated inclusions commonly show multiple
402 bubbles because of the major vesiculation induced by MI depressurization after microcracks nucleation
403 (Lowenstern,1995). Microchemical data were collected on selected inclusions, avoiding those with
404 embayments and significant amounts of Fe-oxides crystallized within decrepitation cracks.

406 **4.4) Microchemical characterization**

407 Mean EMP data (Table 1) show that homogenized inclusions contain a leucogranitic melt, with $\text{SiO}_2 \geq 68$
408 wt%, $\text{Al}_2\text{O}_3 \sim 12\text{-}13$ wt%, variable K_2O and Na_2O , $\text{FeO} \leq 3$ wt% and CaO , $\text{MgO} < 1$ wt%. Fluids content was
409 estimated by EMP difference, and it is variable depending on the case study. The enclosed melt is always
410 peraluminous, as testified by the ASI index ≥ 1.15 . The average maficity of the melt (total iron and
411 magnesium contents expressed as atomic Fe+Mg) is generally low, and increases from 0.026 in Ronda
412 samples to 0.056 in khondalites.

413 In Ronda migmatites, where MI were homogenized at $T = 700^\circ\text{C}$ via piston cylinder, the enclosed melt
414 shows the lowest SiO_2 and the highest volatiles contents (respectively ~ 67 wt% and ~ 8 wt%) among the
415 investigated inclusions. K_2O is only slightly higher than Na_2O (4 wt% vs. 2.5 wt%), even after Na correction
416 (see “methods” paragraph). Re-homogenized MI have a bulk composition very similar to the preserved
417 glassy inclusions in not re-heated samples. Nanogranites from Barun gneisses, re-homogenized via heating
418 stage at $\sim 830^\circ\text{C}$, have higher SiO_2 , ~ 74 wt%, and a lower fluid content, ~ 2.5 wt% and $\text{K}_2\text{O} > \text{Na}_2\text{O}$, 5 wt%
419 vs. 2 wt%. In khondalites the enclosed melt has similar SiO_2 , while fluid content is lower, < 1 wt%, and
420 $\text{K}_2\text{O} \gg \text{Na}_2\text{O}$, 7 vs. 1 wt%. In the latter case the average composition is comparable to those of the preserved
421 glassy inclusions in terms of alkalis contents, confirming the ultrapotassic nature of the trapped melt (Cesare
422 et al., 2009), and fluid content (or EMP totals), while SiO_2 and FeO are respectively lower and higher with
423 respect to glassy inclusions.

424 According to CIPW normative values, the analyzed melts have similar Qz (~ 40), while Ab and Or are
425 variable, with Or from similar to much higher than Ab, depending on the protolith; An is always low, ≤ 4 and

every analyzed melt is corundum-normative. When plotted in a Ab-Qz-Or ternary (Fig. 10) data from each case study define a single cluster, which include the correspondent glassy MI compositions in the case of Ronda migmatites and khondalites. MI compositions plot always above the cotectic curve, in the Qz-bearing field composition, at variable distance from the “minimum melt” composition expected to represent the lowest T composition (at P= 0.5 GPa and $a_{\text{H}_2\text{O}} = 0.5$; Johannes & Holtz, 1996) of a haplogranite melt (see fig. 10). Among the reported data, Ronda melt compositions are the closest to the “minimum”, although with higher Qz component. Barun melts are characterized by the highest normative An value among the considered datasets. Their compositions plot in an intermediate position among Ronda migmatites and khondalites. The latter case study show instead the melt with the highest mean Or, ~4-5 times the Ab value, which plot close to the Qz-Or join, very far from the “minimum melt” composition.

5) Discussion

5.1) Occurrence

The microstructural study confirmed that investigated anatectic MI are primary, i.e. they were trapped during peritectic mineral growth, as testified by their zonal arrangement (Sobolev & Kostyuk, 1975). Anatectic MI have been recognized in garnet and, less commonly, in ilmenite. Both minerals have a large stability field, and are generally more resistant to deformation and microcracking (because of hardness and absence of cleavages) with respect to another common MI-host phase such as quartz, and MI enclosed in them are therefore likely to be preserved during the post-peak trajectory. Among the peritectic phases in the metapelitic system, also spinel may be considered as a reliable host for anatectic MI. Glassy MI containing anatectic melt were reported to occur also in andalusite within crustal xenoliths from Mazarrón, NVP (Cesare et al., 2003) and from Crd-bearing rhyolites of Lipari (Cesare et al., 2011; Di Martino et al., 2011), providing further constraints to the Al_2SiO_5 triple point. Also a mineral phase such as sillimanite, although commonly a reactant in partial melting reactions in metapelitic migmatites, if in excess during partial melting reactions may re-crystallize as prismatic crystals possibly entrapping the anatectic melt, as locally visible in

451 khondalites (E. Salvioli-Mariani, Pers. Comm.). In El Hoyazo enclaves also plagioclase and biotite contain
452 MI, besides garnet and spinel, because both peritectic products of a rapid, disequilibrium melting reaction
453 involving a low grade metapelitic protolith (Cesare and Maineri, 1999). This occurrence suggests that also
454 those phases, commonly regarded as reactants under partial melting conditions, may trap melt in peculiar
455 geological settings characterized by high heating rates, and should be therefore targeted during investigation
456 for anatectic MI.

457 Mineral inclusions of size comparable to MI, mainly accessories (Ap, Rt, Zr), often visible in the
458 investigated inclusions, show features, e.g. large size and mineralogical variability, which rule out the
459 possibility they are daughter phases. These mineral phases are often indented in MI walls, suggesting they
460 were first trapped in the growing host mineral, and then acted as clinging surfaces for the melt, similarly to
461 what happens in igneous rocks (Roedder, 1984). Analogous occurrence was reported in migmatites from the
462 Western Adirondacks Highlands by Henriquez and Darling (2009), where crystallized inclusions in peritectic
463 garnet, interpreted as nanogranites, always contain or cling to a zircon grain. This occurrence suggests that a
464 fine grain-sized protolith containing abundant “inert” accessory phases (graphite, rutile, apatite, zircon,
465 ilmenite) is more likely to favour the MI formation during anatexis.

467 **5.2) Post entrapment changes**

468 *Shape maturation*

469 The negative-crystal shape typically found in anatectic MI is not a primary feature, as confirmed by
470 experiments on fluid inclusion formation in different minerals and artificial crystalline compounds (Maze et
471 al., 1981; Sisson et al., 1993). At HT conditions, such a shape is likely to develop through the host
472 redistribution in a brief span of time, e.g. in less than one year for MI in quartz (e.g. Clocchiatti, 1975;
473 Manley, 1986). This “shape maturation” is commonly observed both in experimental and in natural MI-
474 bearing rocks (Skirius et al., 1990; Lowenstern, 1994) and it represents a process through which the surface
475 free energy is lowered by modifying the inclusion morphology (Roedder, 1984; Lowenstern, 1995). The

476 lowest energy configuration corresponds to a negative-crystal for a melt inclusions, whose shape varies
477 depending on the host crystalline structure, e.g. in garnet-hosted inclusions this means an isometric shape
478 with rhombododecahedral geometry. In MI under investigation shape maturation is likely to predate the
479 beginning of melt crystallization, since mineral phases in them often grow on planar walls.

480 Another example of “shape maturation” is the necking down of former elongate MI, already reported in El
481 Hoyazo enclaves (Acosta-Vigil et al. 2007) and locally observed in Barun samples. The same process may be
482 regarded as the responsible for the occurrence of MI with a well developed negative-crystal shape and a very
483 short mutual distances ($\leq 1 \mu\text{m}$), both in Barun and Ronda samples (see e.g. fig. 14b in Cesare et al., 2011).

485 *Decrepitation*

486 In Barun samples, the most part of MI presents offshoots. Similar microstructures were reported by
487 Stöckhert et al. (2009) in UHP inclusions in garnet of the quartzofeldspathic rocks of Saxonian Erzgebirge,
488 Germany, and interpreted as microcracks produced by MI decrepitation, afterwards in-filled with crystal
489 phases. The presence of offshoots with radial arrangements, often observed in decrepitated FI, support this
490 hypothesis. Moreover, results of re-equilibration studies (see e.g. Bodnar, 2003) show how larger FI are more
491 likely to undergo microcracking, and this is confirmed in Barun case where only smallest MI are preserved.

492 Decrepitated inclusions are extremely abundant in Barun samples, and offshoots also occur in khondalites.
493 The two case studies differ as retrograde P-T-t trajectory, counterclockwise in khondalites and clockwise in
494 Barun gneisses. In the first case a T decrease precedes the drop of the confining pressure, and this largely
495 lowered the MI internal pressure (because of the steep slope of the MI isochore, Lowenstern, 1994), limiting
496 therefore the magnitude of the differential pressure experienced by the MI, and subsequently the extent of
497 decrepitation phenomena. On the contrary, in the second case study depressurization took place after the
498 partial melting event, likely with no appreciable T (and subsequent internal P) decrease, and caused therefore
499 decrepitation of a larger amount of MI.

500 A further difference is related to the common offshoots length, minor in khondalites with respect to Barun
501 samples. In the first case the observed length, $<$ MI radius, corresponds to what expected when MI
502 decrepitate because of the building up of the differential pressure (Tait, 1992). Conversely, in Barun MI the
503 major length of the offshoots, often \gg MI radius, may suggest that, besides overpressurization, MI
504 decrepitation was enhanced also by some other factors, most likely a deformational phase, during the
505 retrograde path, as also suggested by the abundance of microcracks in MI-bearing garnets.

506 Since preserved and decrepitated inclusions have the same phase assemblage, it may be inferred that there
507 were no external fluid infiltrations neither in Barun nor in KKB samples, although decrepitation likely caused
508 the leakage of (at least) part of the fluids from the inclusion. In khondalites, the occurrence of biotite,
509 probably the first mineral phase to precipitate, within the offshoots suggest that decrepitation took place
510 before the beginning of the melt crystallization. It is also possible that decrepitation triggered crystallization,
511 as often recognized in aqueous solutions-bearing FI, where pressure drop causes a solubility drop that leads
512 to daughter phases precipitation (Manning, 2004).

514 **5.3) Re-melting the nanogranites**

515 MI-bearing sample from Barun gneisses and khondalites were re-heated under continuous optical
516 observation, until the crystalline assemblage melted completely. The melting T is interpreted as the minimum
517 T of crystallization of the melt, and is generally assumed as to its trapping temperature (Frezzotti, 2001).
518 Melting temperatures obtained in this work are consistent in the case of Barun gneisses, for which an
519 anatectic event at 800-860°C at 0.8 GPa was proposed (Groppo et al., submitted), while for Khondalites
520 homogenization was reached only at $T > 1000^\circ\text{C}$, a temperature not consistent with those reported in
521 literature, $\sim 900^\circ\text{C}$ (Shabeer et al., 2005).

522 In case of Ronda migmatites, homogenization was obtained through piston cylinder method, and the
523 application of a confining pressure reduced MI decrepitation (and subsequent volatile loss) and Fe oxides
524 formation. Generally the piston cylinder approach gives better results in term of percentage of fully re-

525 homogenized and not decrepitated MI in the clusters. The abundance of preserved MI in the investigated
526 samples is the basic requirement for the choice of this method, although the use of the heating stage remains
527 useful at the preliminary phase of the investigation, since it represents a less time-consuming method to
528 verify if crystallized inclusions may be actually re-melted. In case of less favorable sample the heating stage
529 may however represent the only feasible approach, e.g. for Barun gneisses case study, given the scarcity of
530 preserved inclusions.

531 FESEM investigation showed that, after homogenization, re-melted MI mainly show linear boundaries
532 and, locally, the negative-crystal shapes already observed in nanogranites. This fact suggests that within
533 investigated anatectic MI, or at least a part of them, no host dissolution took place on re-heating. This a
534 remarkable difference with respect to what observed in MI study from igneous rocks, where host re-melting
535 is actually expected, in order to bring back the melt to its original composition. In fact, it is normally
536 observed that, during cooling, host crystallizes on MI walls, with variable amounts depending on the case
537 study (e.g. Frezzotti, 2001). The lack of host-crystallization in anatectic MI is easier to be verified when they
538 occur in host minerals which do not belong to the phase assemblage expected for a nanogranite, e.g. garnet.
539 Vice-versa, in case of MI trapped in peritectic plagioclase or K-feldspar, both phases are likely to be also
540 crystallization products of the enclosed anatectic melt, and the resultant overgrowth on MI walls may result
541 hardly distinguishable from the original host, mainly because of the investigation scale.

543 **5.4) Compositions of the anatectic melt**

544 The bulk composition obtained by EMP analyses is peraluminous and leucogranitic, with variable alkali
545 contents depending on the case study. In the Ab-Qz-Or ternary diagram the collected datasets define three
546 different clusters, whose positions is always in the Qz-bearing field, at variable distance from the “minimum
547 melt” composition (Johannes & Holtz, 1996).

548 From a general point of view, experimental data on haplogranitic system and natural rocks represent a
549 valid frame to handle the compositional datasets made available by the investigation of anatectic MI. For

550 example, when the different melts are compared, the average normative Ab, decreasing from ~25 to 10 in
551 Ronda and KKB melts respectively, is negatively correlated with the increasing temperature of formation, in
552 agreement with higher melting temperatures reported in literature for Na-poor haplogranite melts (e.g.
553 Johannes & Holtz, 1996). Also volatile contents are consistent with the inferred conditions of partial melting,
554 in fact MI from Ronda, likely to have been trapped at ~700 °C (Tajcmanova et al., 2011) show the highest
555 amount of fluid (~8 wt%), while KKB melts, generated at T>900, are almost dry. In Barun and KKB
556 samples, however, the inferred fluid contents are likely to represent minimum values, because of the
557 widespread evidence of decrepitation and vesiculation among re-melted MI after heating runs.

558 The average FeO and Na₂O of KKB inclusions is similar to the values reported in literature for
559 peraluminous granites (Droop et al., 2003) produced by partial melting of natural rocks at 900°C and 0.5
560 GPa, suggesting therefore that the relatively high FeO and low Na₂O contents can be a primary feature of the
561 anatectic melt. That being so, both the objections raised by Clemens (2009) whether or not the trapped phase
562 was anatectic melt and on the quality of the geochemical data in Cesare et al. (2009), in particular about the
563 applied Na-loss correction, can be considered definitely untenable.

564 The maficity index slightly increases with the melting temperature and is always low and comparable with
565 a pristine S-type leucogranite compositions, e.g. subvolcanic bodies in the Cape Granite Suite reported by
566 Stevens et al. (2007). Investigated melts should be therefore considered as examples of the “starting“ magma
567 which, migrating upward and incorporating variable amounts of peritectic phases (Stevens et al., 2007), will
568 be emplaced at shallower crustal levels forming S-type granitic bodies with large compositional variability
569 (Villaros et al., 2009a;b).

570 An important point that needs to be addressed is whether or not the trapped melt is representative of the
571 bulk anatectic melt in the investigated rocks. Acosta-Vigil et al., (2007, 2010) reported the occurrence of
572 disequilibrium phenomena in anatectic MI from El Hoyazo enclaves, but also showed how disequilibrium
573 affects only the concentrations of the compatible trace elements and not those of major and incompatible
574 trace elements. In the present study, microchemical data on major elements in anatectic MI are therefore

575 likely to be considered as representative of the bulk composition of the original anatectic melt, also in terms
576 of Na content, after the application of correction factors (if needed) calculated using the appropriate glass
577 standards (see “methods”).

578 Re-melted MI compositions are comparable with the correlated glassy MI (Fig. 10; Table 1), supporting
579 the hypothesis that clusters contain inclusions of the same melt, despite the different degree in crystallization
580 revealed by the microstructural investigation. This evidence, coupled with their texturally primary nature,
581 rules out the possibility, proposed by Clemens (2009), that glassy inclusions may represent later-infiltrated
582 silica-rich fluids with respect to nanogranites. Moreover, silica-rich fluids may occur in UHP terrains (e.g.
583 Stöckhert et al., 2009; Malaspina et al., 2006) but they commonly have a phase assemblage characterized by
584 hydrous mineral phases, i.e. phyllosilicates and amphiboles, very different with respect to the nanogranite
585 assemblage. Moreover, the fluid content in investigated anatectic MI is 2 -10 wt%, notably lower than the
586 fluid in common silica-rich inclusions, e.g. 25-50 wt% (Frezzotti et al., 2007).

587 Since the enclosed melt composition is comparable, the different behavior on crystallization is unexpected.
588 The most reliable hypothesis involves a pore size effect on the phase nucleation in the melt, based on a
589 statistical study of MI size in khondalites (8 and 13 μm for preserved glassy and nanogranite inclusions
590 respectively, Cesare et al., 2009), suggesting that phase solubility (or the threshold supersaturation) is higher
591 in smaller pores (Putnis et al., 1995). This is related to the highest interfacial energy of the crystals in smaller
592 pores with respect to larger ones, which promotes and accelerate crystal dissolution in melt volumes with
593 diameter $\leq 10 \mu\text{m}$ (Immanuel et al., 2009). The occurrence of glassy MI in Ronda migmatites with size often
594 equal to, or larger than, nanogranites is however puzzling and cannot be explained only with the pore size
595 effect, but rather with the heterogeneous distribution of nucleation sites in inclusions with a threshold
596 diameter (Cesare et al., 2011).

598 **6) Conclusions**

599 Melt inclusions occur in garnet, and locally also in ilmenite, within partially-melted metasedimentary
600 rocks from Ronda migmatites, Barun gneisses and KKB. Data here presented along with previous works
601 (Cesare et al., 2009; 2011), support the hypothesis that investigated inclusions formed during peritectic phase
602 growth and contain the melt generated by crustal melting. The microstructural study revealed the occurrence
603 of a leucogranitic phase assemblage formed by quartz, feldspar(s), biotite and/or muscovite \pm accessories
604 within completely crystallized MI (*nanogranites*). A peculiar feature is represented by the variable degree of
605 crystallization within the same cluster, where nanogranites coexist with partially crystallized and glassy
606 inclusions. Normally MI show post-entrapment changes such as shape maturation, resulting in a more or less
607 developed negative crystal shape, and necking down phenomena, which however did not modify the original
608 melt composition. No external fluid infiltration is visible in the decrepitated inclusions, which show the same
609 mineralogical assemblage of preserved nanogranites.

610 Microchemical data on re-melted anatectic MI are considered representative of the enclosed melt, since the
611 Na-loss was corrected by using standard glasses of compositions similar to the analyzed melts. The resultant
612 composition is generally peraluminous and leucogranitic, as suggested by experimental melting of
613 metapelites and metagraywackes. The similarity of melts in different inclusions (in the same case study) rules
614 out the presence of phenomena such as boundary layer effects and local disequilibrium, implying therefore
615 that the investigated melt can be considered as representative of the original anatectic melt. Compositional
616 data give further support to the hypothesis that MI with different crystallization degrees contain the same
617 melt, and subsequently glassy inclusions did not form after the nanogranites (as suggested by Clemens, 2009)
618 but at the same time. The microstructural investigation showed that melt entrapment, with subsequent MI
619 formation, is more probable in fine grained protoliths, as suggested by the abundance of small-size trapped
620 minerals. So far inclusions have been recognized to occur in minerals more resistant to deformation, e.g.
621 garnet and ilmenite, and because of the similar features also spinel may be regarded as a suitable host for
622 anatectic MI.

623 MI may be also regarded as valuable microstructural evidence for the presence of melt, especially because,
624 being sheltered by the host phase, they are likely to survive retrograde modifications re-crystallization and
625 also further metamorphic cycles, which commonly obliterate other melt witnessing microstructure.

626 Anatectic melt inclusions represents a powerful approach to the characterization of the original melt
627 produced by partial melting within natural samples, before it undergoes modifications commonly observed in
628 leucosomes. Furthermore, they allow the comparison between melt in natural rocks and experimental
629 datasets, already available on natural samples and synthetic compositions. The study of anatectic MI poses
630 severe technical problems, and requires the use of very high-resolution techniques to obtain valuable
631 microstructural and microchemical data. However, now available technologies allow us to face and overcome
632 these challenges, moving further our comprehension of the partial melting processes in metapelites and
633 metagraywackes, and subsequently the evolution of an important portion of the continental crust during
634 orogenic cycles.

635 **ACKNOWLEDGEMENTS**

637 The present paper contains part of the results of the PhD thesis of the SF and OB. The authors wish to thank
638 Stephen McCartney (ICTAS, Virginia Tech) for assistance during elemental mapping. Robert J. Bodnar,
639 Antonio Acosta-Vigil, Maria-Luce Frezzotti, Robert Tracy and Rosario Esposito are also acknowledged for
640 their helpful discussions. Financial support for this project came from the Italian Ministry of Education,
641 University, Research (grant PRIN 2007278a22 to BC) and a Research grant from Fondazione “Aldo Gini” to
642 SF.

643 **REFERENCES**

645 Acosta-Vigil, A., Buick, I., Hermann, J., Cesare, B., Rubatto, D., London, D. & Morgan VI, G., 2010.
646 Mechanisms of crustal anatexis: a geochemical study of partially melted metapelitic enclaves and host dacite,
647 SE Spain. *Journal of Petrology*, **51**, 785-821.

648 Acosta-Vigil, A., Cesare, B., London, D., Morgan VI, G.B., 2007. Microstructures and composition of
649 melt inclusions in a crustal anatectic environment, represented by metapelitic enclaves within El Hoyazo
650 dacites, SE Spain. *Chemical Geology*, **235**, 450–465.

651 Acosta-Vigil, A., London, D., Morgan VI, G.B. & Dewers, T.A., 2003. Solubility of excess alumina in
652 hydrous granitic melts in equilibrium with peraluminous minerals at 700–800°C and 200 MPa, and
653 applications of the aluminum saturation index. *Contributions to Mineralogy and Petrology*, **146**, 100–119.

654 Acosta-Vigil, A., Pereira, M.D., Shaw, D.M. & London, D., 2001. Contrasting behaviour of boron
655 during crustal anatexis. *Lithos*, **56**, 15-31.

656 Anderson, A.T., Jr., 1974, Evidence for a picritic, volatile-rich magma beneath Mt. Shasta, California.
657 *Journal of Petrology*, **15**, 243-267.

658 Bodnar, R.J., 2003. Re-equilibration of fluid inclusions. In: *Fluid Inclusions: Analysis and Interpretation*
659 (eds Samson, I., Anderson, A. & Marshall, D.) pp 213-230. Mineralogical Association of Canada, Short
660 Course 32.

661 Bodnar, R.,J., Student, J.J., 2006. Melt inclusions in plutonic rocks: petrography and microthermometry.
662 In: *Melt inclusions in plutonic rocks* (ed Webster, J.D.), pp. 1-26. Mineralogical Association of Canada,
663 Short Course 36.

664 Bordet, P. (1961). Recherches géologiques dans l’Himalaya du Népal, région du Makalu. Editions du
665 Centre National de la Recherche Scientifique, Paris, 275 p.

666 Braga, R. & Massonne, H.J., 2008. Mineralogy of inclusions in zircon from high-pressure crustal rocks
667 from the Ulten Zone, Italian Alps. *Periodico di Mineralogia*, **77**, 43–64.

668 Braun, I., Raith, M. & Ravindra Kumar, G. R., 1996. Dehydration-melting phenomena in leptynitic
669 gneisses and the generation of leucogranites: a case study from the Kerala Khondalite Belt, southern India.
670 *Journal of Petrology*, **37**,1285–1305.

671 Brown, M., Rushmer, T., 2006. Evolution and Differentiation of the Continental Crust. Cambridge
672 University Press, Cambridge, 553p.

673 Carrington, D.P. & Harley, S.L., 1995. Partial melting and phase relations in high-grade metapelites: an
674 experimental petrogenetic grid in the KFMASH system. *Contribution to Mineralogy and Petrology*, **120**,
675 270–291.

676 Cenkı, B., Kriegsman, L. M. & Braun, I., 2002. Melt-producing and melt-consuming reactions in
677 anatectic granulites: P-T evolution of the Achankovil cordierite gneisses, South India. *Journal of*
678 *Metamorphic Geology*, **20**, 543-561.

679 Cesare, B., Acosta-vigil, A., Ferrero, S. & Bartoli, O., 2011. Melt inclusions in migmatites and
680 granulites. In: *Journal of the Virtual Explorer* (Eds Forster, M.A. & Fitz Gerald, J.D.), n. 2. Doi:
681 10.3809/jvirtex.2011.00268.

682 Cesare, B., Ferrero, S., Salvioli-Mariani, E., Pedron, D. & Cavallo, A., 2009. Nanogranite and glassy
683 inclusions: the anatectic melt in migmatites and granulites. *Geology*, **37**, 627-630.

684 Cesare, B. & Maineri, C., 1999. Fluid-present anatexis of metapelites at El Joyazo (SE Spain):
685 constraints from Raman spectroscopy of graphite. *Contributions to Mineralogy and Petrology*, **135**, 41–52.

686 Cesare, B., Maineri, C., Baron Toaldo, A., Pedron, D. & Acosta-Vigil, A., 2007. Immiscibility between
687 carbonic fluids and granitic melts during crustal anatexis: a fluid and melt inclusion study in the enclaves of
688 the Neogene Volcanic Province of SE Spain. *Chemical Geology*, **237**, 433-449.

689 Cesare, B., Marchesi, C., Hermann, J. & Gomez-Pugnaire, M.T. , 2003. Primary melt inclusions in
690 andalusite from anatectic graphitic metapelites: Implications for the position of the Al₂SiO₅ triple point.
691 *Geology*, **31**, 573-576.

692 Cesare, B., Salvioli Mariani, E. & Venturelli, G., 1997. Crustal anatexis and melt extraction during
693 deformation in the restitic xenoliths at El Joyazo (SE Spain). *Mineralogical Magazine*, **61**, 15–27.

694 Cesare, B. & Gomez-Pugnaire, M.T., 2001. Crustal melting in the Alborán domain: constraints from the
695 xenoliths of the Neogene Volcanic Province. *Physics and Chemistry of the Earth*, **26**, 255–260.

696 Cesare, B., 2008. Crustal melting: working with enclaves. In: *Working with Migmatites* (eds Sawyer,
697 E.W. & Brown, M.), pp. 37–55. Mineralogical Association of Canada, Short Course 38.

698 Chacko, T., Ravindra-Kumar, G. R. & Newton, R. C., 1987. Metamorphic P-T conditions of the Kerala
699 (S. India) Khondalite belt, a granulite facies supracrustal terrain. *Journal of Geology*, **95**, 343–358.

700 Chacko, T., Lamb, M. & Farquhar, J., 1996. The Archean and Proterozoic terrains in southern India
701 within East Gondwana. In: *Gondwana Research Group Memoir 3* (eds Santosh, M. & Yoshida, M.), pp.
702 157–165. Field Science, Osaka.

703 Clemens, J.D., 2009. The message in the bottle: “Melt” inclusions in migmatitic garnets. *Geology*, **37**,
704 671–672.

705 Clocchiatti, R., 1975, Les inclusions vitreuses des cristaux de quartz. Étude optique, thermo-optique et
706 chimique. Applications géologiques. *Mémoires de la Société géologique de France*, **122**, 1-96.

707 Collins, A.S. & Windley, B.F., 2002. The tectonic evolution of central and northern Madagascar and its
708 place in the final assembly of Gondwana. *Journal of Geology*, **110**, 325–339.

709 Droop, G.T.R., Clemens, J.D. & Dalrymple, J., 2003. Processes and conditions during contact anatexis,
710 melt escape and restite formation: the Huntly Gabbro complex, NE Scotland. *Journal of Petrology*, **44**, 995-
711 1029.

712 Di Martino, C., Forni, F., Frezzotti, M.L., Palmeri, R., Webster, J., Ayuso, R., Lucchi, F., & Tranne, C.,
713 2011. Formation of cordierite-bearing lavas during anatexis in the lower crust beneath Lipari Island (Aeolian
714 arc, Italy). *Contributions to Mineralogy and Petrology*, in press. Doi: 10.1007/s00410-011-0637-0.

715 Emmanuel, S., Ague, J.J. & Walderhaug, O., 2010. Interfacial energy effects and the evolution of pore
716 size distributions during quartz precipitation in sandstone. *Geochimica et Cosmochimica Acta*, **74**, 3539-
717 3552. DOI: 10.1016/j.gca.2010.03.019.

718 Esteban, J.J., Cuevas, J., Vegas, Tubia, J.M., 2008. Deformation and kinematics in a melt-bearing shear
719 zone from the Western Betic Cordilleras (Southern Spain). *Journal of Structural Geology*, **30**, 380-393.

720 Esteban, J.J., Sanchez-Rodriguez, L., Seward, D., Cuevas, J. & Tubia, J.M., 2004. The late thermal
721 history of the Ronda area. *Tectonophysics*, **389**, 81-92.

722 Ferrero, S., Bodnar, R.J., Cesare, B. & Viti, C., 2011. Re-equilibration of primary fluid inclusions in
723 peritectic garnet from metapelitic enclaves, El Hoyazo, Spain. *Lithos*, **124**, 117-131. DOI:
724 10.1016/j.lithos.2010.09.004.

725 Frezzotti, M.L., 2001. Silicate melt inclusions in magmatic rocks: applications to petrology. *Lithos*, **55**,
726 273–299.

727 Frezzotti, M.L., Ghezzi, C. & Stefanini, B., 1992. The Calabona intrusive complex, Sardinia Italy:
728 evidence for a porphyry-copper system. *Economic Geology*, **87**, 201–212.

729 Frezzotti, M.L., Ferrando, S., Dallai, L. & Compagnoni, R. 2007. Intermediate Alkali-Alumino-silicate
730 Aqueous Solutions Released by Deeply Subducted Continental Crust: Fluid Evolution in UHP OH-
731 rich Topaz-Kyanite Quartzites from Donghai (Sulu, China). *Journal of Petrology*, **48**, 1219-1241.

732 Gardien, V., Thompson, A.B., Grujic, D., Ulmer, P., 1995. Experimental melting of biotite + plagioclase
733 + quartz ± muscovite assemblages and implications for crustal melting. *Journal of Geophysical Research*,
734 **100**, 15581–15591.

735 Goscombe, B. & Hand, M. (2000). Contrasting P-T paths in the Eastern Himalaya, Nepal: inverted
736 isograds in a paired metamorphic mountain belt. *Journal of Petrology*, **41**, 1673–1719

737 Groppo, c., Rolfo, F. & Indares, A., 2011. Partial melting in the Higher Himalayan Crystallines of
738 Eastern Nepal: implications for the “channel flow” model. *Journal of Petrology*, submitted.

739 Halter, W.E., Pettke, T., Heinrich, C.A. & Rothen-Rütishauser, B., 2002. Major to trace element analysis
740 of melt inclusions by laser-ablation ICP-MS: methods of quantification. *Chemical Geology*, **183**, 63–86.

741 Hartel, T. H. D., Pattison D. R. M., Helmers, H. & Maaskant, P., 1990. Primary granitoid-composition
742 inclusions in garnet from granulite facies metapelite: Direct evidence for the presence of a melt? *Geological
743 Association of Canada* **15**, 54 (abstract).

744 Henriquez, J.L. & Darling, R.S., 2009. Zircon-clinging inferred anatectic melt inclusions in Adirondack
745 Garnet.. Northeastern Section (45th Annual) and Southeastern Section (59th Annual) Joint Meeting, 13-16
746 March 2010 (abstract).

747 Holness, M.B. & Sawyer, E.W., 2008, On the pseudomorphing of melt-filled pores during the
748 crystallization of migmatites. *Journal of Petrology*, **49**, 1343–1363.

749 Johannes, W., Holtz, F., 1996. Petrogenesis and experimental petrology of granitic rocks. Berlin,
750 Springer, 335pp.

751 Lowenstern, J.B., 1994. Chlorine, fluid immiscibility, and degassing in peralkaline magmas from
752 Pantelleria, Italy. *American Mineralogist*, **79**, 353-369.

753 Lowenstern, J., 1995. Applications of silicate-melt inclusions to the study of magmatic volatiles. In:
754 *Magmas, Fluids and Ore Deposits* (ed Thompson, J.F.H.), pp. 71-99. Mineralogical Association of Canada
755 Short Course, 23.

756 Lowenstern, J.B., 2003. Melt inclusions come of age: volatiles, volcanoes, and Sorby's legacy. In: *Melt*
757 *Inclusions in Volcanic Systems: Methods, Applications and Problems* (eds De Vivo, B. & Bodnar, R.J.), pp.
758 1–22. *Developments in Volcanology*, 5, Elsevier Press, Amsterdam,.

759 Malaspina, N., Hermann, J., Scambelluri, M. & Compagnoni, R., 2006. Polyphase inclusions in garnet-
760 orthopyroxenite (Dabie Shan, China) as monitors for metasomatism and fluid-related trace element transfer
761 in subduction zone peridotite. *Earth and Planetary Science Letters*, **249**, 173-187. DOI:
762 10.1016/j.epsl.2006.07.017.

763 Manley, C.R., 1996. Morphology and maturation of melt inclusions in quartz phenocrysts from the
764 Badlands rhyolite lava flow, southwestern Idaho. *American Mineralogist*, **81**, 158-168.

765 Manning, C.E., 1994. The solubility of quartz in H₂O in the lower crust and upper mantle. *Geochimica et*
766 *Cosmochimica Acta*, **58**, 4831-4839.

767 Marchildon, N. & Brown, M., 2001. Melt segregation in late syn-tectonic anatectic migmatites: An
768 example from the Onawa contact aureole, Maine, USA. *Physics and Chemistry of the Earth, Part A: Solid*
769 *Earth and Geodesy*, **26**, 225–229.

770 Maze, W.B., Bergman, S.C., & Sisson, V.B., 1981. Direct observations of the formation of fluid primary
771 inclusions. *Geological society of America abstracts with programs*, **13**, 506.

772 Melson, W.G., 1983, Monitoring the 1980-1982 eruptions of Mount St. Helens: Compositions and
773 abundances of glass. *Science*, **221**, 1387-1391.

774 Morgan VI, G.B., London, D., 1996. Optimizing the electron microprobe analysis of hydrous alkali
775 aluminosilicate glasses. *American Mineralogist*, **81**, 1176–1185.

776 Morgan, G.B., IV, London, D., 2005, Effect of current density on the electron microprobe analysis of
777 alkali aluminosilicate glasses. *American Mineralogist*, **90**, 1131–1138.

778 Nandakumar, V. & Harley, S.L., 2000. A reappraisal of the pressure-temperature path of granulites from
779 the Kerala Khondalite Belt, Southern India. *Journal of Geology*, **108**, 687–703.

780 Patiño-Douce, A.E. & Harris, N., 1998. Experimental Constraints on Himalayan Anatexis. *Journal of*
781 *Petrology*, **39**, 689-710.

782 Platt, J.P. & Whitehouse, M.J., 1999. Early Miocene high-temperature metamorphism and rapid
783 exhumation in the Betic Cordillera (Spain): evidence from U–Pb zircon ages. *Earth Planetary Science*
784 *Letters*, **171**, 591–605.

785 Platt, J.P., Whitehouse, M.J., Kelley, S.P., Carter, A. & Hollick, L., 2003. Simultaneous extensional
786 exhumation across the Alboran Basin: Implications for the causes of late orogenic extension. *Geology*, **31**,
787 251–254.

788 Putnis, A., Prieto, M. & Fernandez-Diaz, L., 1995. Fluid supersaturation and crystallization in porous
789 media. *Geological Magazine*, **132**, 1–13.

790 Roeder, E., 1979. Origin and significance of magmatic inclusions. *Bulletin of Mineralogy*, **102**, 487-
791 510.

792 Roedder, E., 1984, Fluid inclusions. Mineralogical Society of America, Reviews in Mineralogy, 12,
793 644p.

794 Sanchez-Rodriguez, L., 1998. Pre-Alpine and Alpine evolution of the Ronda Ultramafic Complex and its
795 country-rocks Betic chain, southern Spain.: U–Pb SHRIMP zircon and fission-track dating. Published PhD
796 Thesis, ETH Zürich, 170 pp.

797 Santosh, M., 1986. Cordierite gneisses of southern Kerala, India: petrology, fluid inclusions and
798 implications for crustal uplift history. *Contributions to Mineralogy and Petrology*, **96**,343–356.

799 Sato, K., Miyamoto, T., & Kawasaki, T., 2004. Experimental constraints of metamorphic pressure and
800 temperature, and phase relations of a phlogopite-bearing orthopyroxene granulite from Howard Hills, Napier
801 Complex, East Antarctica. *Journal of Mineralogical and Petrological Sciences*, **99**, 191-200.

802 Sawyer, E.W., 1996. Melt-segregation and magma flow in migmatites: implications for the generation of
803 granite magmas. *Transactions of the Royal Society of Edinburgh. Earth Sciences*, **87**, 85–94.

804 Sawyer, E.W., 2008, Atlas of Migmatites. Mineralogical Association of Canada, The Canadian
805 Mineralogist Special Publication 9, 386p.

806 Shabeer, K.P., Satish-Kumar, M., Armstrong, R. & Buick, I. S., 2005. Constraints on the timing of Pan-
807 African granulite-facies metamorphism in the Kerala Khondalite Belt of southern India: SHRIMP mineral
808 ages and Nd isotopic systematics. *Journal of Geology*, **113**, 95-106.

809 Sisson, V.B., Lovelace, R.B., Maze, W.B. & Bergman, S.C., 1993. Direct observation of primary fluid-
810 inclusion formation. *Geology*, **21**, 751-754.

811 Skirius, C.M., Peterson, J.W. & Anderson, A.T. Jr., 1990. Homogenizing rhyolitic glass inclusions from
812 the Bishop Tuff. *American Mineralogist*, **75**, 1381-1398.

813 Sobolev, A.V., 1996. Melt inclusions in minerals as a source of principle petrological information.
814 *Petrology*, **4**, 209-220.

815 Sobolev, V.S. & Kostyuk, V.P., 1975. Magmatic crystallization based on a study of melt inclusions.
816 *Fluid Inclusions Research*, **9**, 182-253 (translated from original publication in Russian).

817 Sorby, H.C., 1858. On the microscopical structure of crystals, indicating origin of minerals and rocks.
818 *Quarterly Journal of the Geological Society of London*, **14**, 453–500.

819 Stevens, G., Clemens, J.D., Droop, T.R., 1997. Melt production during granulite-facies anatexis:
820 experimental data from “primitive” metasedimentary protoliths. *Contributions to Mineralogy and Petrology*,
821 **128**, 352–370.

822 Stevens, G., Villaros, A. & Moyen, J.F., 2007. Selective peritectic garnet entrainment as the origin of
823 geochemical diversity in S-type granites. *Geology*, **35**, 9–12. doi:10.1130/G22959A.1.

824 Stockhert, B., Trepmann, C.A. & Massonne H.J., 2009. Decrepitated UHP fluid inclusions: about diverse
825 phase assemblages and extreme decompression rates (Erzgebirge, Germany). *Journal of Metamorphic
826 Geology*, **27**, 673–684.

827 Student, J.J. & Bodnar, R.J., 1996. Melt inclusion microthermometry: Petrologic constraints from the
828 H₂O-saturated haplogranite system. *Petrology*, **4**, 291-306.

829 Student, J.J. & Bodnar, R.J., 2004. Silicate melt inclusions in porphyry copper deposits: Identification
830 and homogenization behaviour. *Canadian Mineralogist*, **42**, 1563-1600.

831 Tait, S., 1992. Selective preservation of melt inclusions in igneous phenocrysts. *American Mineralogist*,
832 **77**, 146-155.

833 Tajcmanova, L., Bartoli, O., Cesare, B., Acosta-Vigil, A., 2011. Constraining the P-T conditions of
834 melting in stromatic migmatites from Ronda (S Spain). Goldschmidt August 14-19, 2011 in Prague, Czech
835 Republic(abstract).

836 Thomas, R., Rhede, D., & Trumbull, R.B., 1996. Microthermometry of volatile-rich silicate melt
837 inclusions in granitic rocks. *Zeitschrift für Geologische Wissenschaften*, **24**, 505-526.

838 Thompson, A.B., 1982. Dehydration melting of pelitic rocks and the generation of H₂O-undersaturated
839 granitic liquids. *American Journal of Sciences*, **282**, 1567-1595.

840 Tomilenko, A.A. & Chupin V.P., 1983. Studying Inclusions in Minerals from Metamorphic Complexes
841 (Nauka), Novosibirsk, 524pp.

842 Torres-Roldan, R.L., 1983. Fractionated melting of metapelite and further crystal–melt equilibria. The
843 example of the Blanca Unit migmatite complex, north of Estepona _ southern Spain. *Tectonophysics*, **96**, 95–
844 123.

845 Touret, J. & Olsen, S.N., 1985. Fluid inclusions in migmatites. In: *Migmatites* (ed Ashworth, J.R.), pp.
846 265-288, Blackie, Chapman and Hall, New York.

847 Tubía, J.M., Cuevas, J., 1986. High-temperature emplacement of the Los Reales peridotite nappe _Betic
848 Cordillera, Spain. *Journal of Structural Geology*, **8**, 473–482.

849 Tubía, J.M., Cuevas, J. & Gil-Ibarguchi, J.I., 1997. Sequential development of the metamorphic aureole
850 beneath the Ronda peridotites and its bearing on the tectonic evolution of the Betic Cordillera.
851 *Tectonophysics*, **279**, 227–252.

852 Vernon, R. H., 2004. A Practical Guide to Rock Microstructure. Cambridge University Press,
853 Cambridge, 594 pp.

854 Vernon, R.H., 2011. Microstructures of melt-bearing regional metamorphic rocks. In: *Origin and*
855 *Evolution of Precambrian High-Grade Gneiss Terranes, with Special Emphasis on the Limpopo Complex of*
856 *Southern Africa* (eds Van Reenen, D.D., Kramers, J.D., McCourt, S., & Perchuk, L.L.), pp. 1-11. Geological
857 Society of America Memoir, **207**. Doi: 10.1130/2011.1207(01)

858 Vielzeuf, D., Clemens, J.C., Pin, C. & Moinet, E., 1990. Granites, granulites and crustal differentiation.
859 In: *Granulites and Crustal Differentiation* (eds Vielzeuf, D. & Vidal, P.), pp. 59–85. Kluwer Academic
860 Publishers Dordrecht.

861 Vielzeuf, D. & Holloway, J.R., 1988. Experimental determination of the fluid-absent melting relations in
862 the pelitic system. *Contribution to Mineralogy and Petrology*, **98**, 257-276.

863 Villaros, A., Stevens, G. & Buick, I.S., 2009. Tracking S-type granite from source to emplacement: clues
864 from garnet in the Cape Granite Suite. *Lithos*, **112**, 217–235.

865 Villaros, A., Stevens, G., Moyen, J.F. & Buick, I.S., 2009. The trace element compositions of S-type
866 granites: evidence for disequilibrium melting and accessory phase entrainment in the source. *Contributions to*
867 *mineralogy and petrology*, **158**, 543-561. Doi: 10.1007/s00410-009-0396-3

868 Viskupic, K., & Hodges, K.V., 2001. Monazite-xenotime thermochronometry: methodology and an
869 example from the Nepalese Himalaya. *Contributions to Mineralogy and Petrology*, **141**, 233-247. Doi:
870 10.1007/ s004100100239.

871 Webster, J.D., 2006. Melt inclusions in plutonic rocks. Short Course Series, 36. Mineralogical
872 Association of Canada, Quebec, p. 237.

873 Webster, J.D. & Thomas, R., 2006. Silicate melt inclusions in felsic plutons: a synthesis and a review. In:
874 *Melt inclusions in plutonic rocks* (ed Webster, J.D.), pp. 165-188. Short Course Series, 36, Mineralogical
875 Association of Canada, Quebec.

876

877

878 **Figure captions**

879 **Figure 1:** Field aspect of the investigated rocks and microstructural evidences of the former presence of
880 melt in the MI-bearing investigated rocks. (a) Coarse-to-medium grain sized khondalites outcropping at
881 Koliakkode quarry, KKB. *Camera cap= 8 cm*; (b) Fine-grained metatexites at Ronda. *Pen length= 8 cm*; (c)
882 Thin section aspect of khondalites, plane-polarized light. On the left part of the image, Qtz+Kfs bearing
883 leucosome is visible. *Red box*: location of MI cluster; (d) Quartz crystallized as a melt pseudomorph in
884 khondalites (*white arrow*), at crossed polars; (e) Subhedral garnet from Ronda metatexites surrounded by
885 plagioclase crystallized as a melt pseudomorph (*white arrow*) at crossed polars; (f) Same image of (e) at
886 plane-polarized light, MI occur at the core of the garnet; (g) Detail of a skeletal garnet from Barun gneisses at
887 crossed polars, with plagioclase forming a melt pseudomorph (*white arrow*); (h) Same image of (g) at
888 crossed polars.

889

890 **Figure 2:** Examples of garnet hosts, with MI cluster positions (*red boxes*), in plane-polarized light. (a)
891 Large anhedral porphyroblasts in Bt-rich melanosome in khondalites; (b) Subhedral garnet porphyroblasts in
892 Ronda metatexites; (c) Skeletal garnet porphyroblasts in Barun gneisses; (d) Close-up of MI cluster in
893 khondalites; (e) Close-up of MI cluster in Ronda samples; (f) Close-up of MI occurrence in Barun gneisses.
894 *White arrows*: two different clusters of MI characterized by different average size.

895

896 **Figure 3:** Ilmenite grain containing primary MI with azonal arrangement, SEM image.

897

898 **Figure 4:** Photomicrographs of anatectic melt inclusions. (a) and (b) Parallel and crossed polars images of
899 a crystallized inclusion in khondalites; (c) and (d) Parallel and crossed polars images of crystallized and
900 glassy MI coexisting in the same cluster; the single birefringent mineral within the glassy MI is an accessory
901 mineral, most likely an apatite; (e) and (f) Parallel and crossed polars images of a crystallized inclusion with
902 large birefringent phases in Barun gneisses; (g) Crystallized inclusions with symmetrically developed

903 offshoots in khondalites, plane-polarized light; (h) Glassy inclusion in khondalites with a rutile needle
904 indented in the host garnet, plane-polarized light; (i) and l) Parallel and crossed polars images of a
905 crystallized inclusion in Ronda metatexites, (m) and (n) Parallel and crossed polars images of two
906 crystallized inclusions in Barun gneisses, connected by an offshoots filled with birefringent minerals (*white*
907 *arrow*). In lower portion of the picture a preserved crystallized inclusion is visible.

908

909 **Figure 5:** BSE images of anatectic melt inclusions. (a) Nanogranite in khondalites, with a well developed
910 negative crystal shape; (b) Nanogranite in Barun gneisses with a perfectly developed negative crystal shape;
911 (c) Nanogranite with offshoots from Barun gneisses, with cuneiform-shaped quartz intergrown with
912 plagioclase; (d) Crystallized and partially crystallized MI with large rutile needles, likely to have favored the
913 melt entrapment, in Ronda mylonitic migmatites; (e) Typical occurrence of nanogranite in Ronda
914 metatexites; (f) large nanogranite with offshoot in khondalites. *Red box:* K-feldspar elongated grains in
915 quartz; (g) Partially crystallized MI in khondalites. *Red dashed line:* interface residual melt-crystallized
916 phases; (h) Typical occurrence of glassy MI in khondalites, characterized by a perfectly developed negative
917 crystal shape, with a trapped mineral.

918

919 **Figure 6:** X-rays elemental maps on anatectic MI. (a) Large nanogranite from Barun gneisses, the same of
920 fig. 3e, with the typical phase assemblage, and a trapped apatite grain; (b) Nanogranite in khondalites with a
921 micrographic intergrowth of quartz + Kfeldspar.

922

923 **Figure 7:** X-rays map of a partially crystallized MI in khondalites, with Na, Ca and Cl showing the same
924 distribution. *Red arrow:* cuscate-lobate shape of the residual melt around a biotite grain.

925

926 **Figure 8:** (a) Nanogranite from Barun gneisses, characterized by offshoots with radial arrangement typical
927 of decrepitated inclusions. *White arrow:* offshoots with crystallized phases within; (b) Hourglass MI which

928 underwent a partial necking down in Barun gneisses. *Black arrow*: point of development of the bottle neck
929 that precedes the complete separation.

930

931 **Figure 9:** SEM images of re-homogenized nanogranites. (a) Fully homogenized nanogranite in garnet
932 from Ronda migmatites; (b) Homogenized nanogranite from Barun gneisses, characterized by multiple
933 shrinkage bubbles (*white arrows*).

934

935 **Figure 10:** Mean compositions of anatectic MI reported in a CIPW Ab-Qz-Or diagram (see legend).
936 Cotectic curves and minimum melting points for 0.5, 1 GPa are from Johannes & Holtz (1996) for a
937 haplogranite composition at $a_{\text{H}_2\text{O}} = 0.5$ are reported for comparison. *Black symbols*: re-homogenized
938 nanogranites; *gray symbols*: preserved glassy inclusions, where present. *Dashed/dotted lines*: distributions of
939 the retrieved compositions for each case study.

940

941 **Table 1:** EMP analyses of homogenized and preserved glassy MI (where present), reported for
942 comparison. All Fe considered as Fe^{2+} .

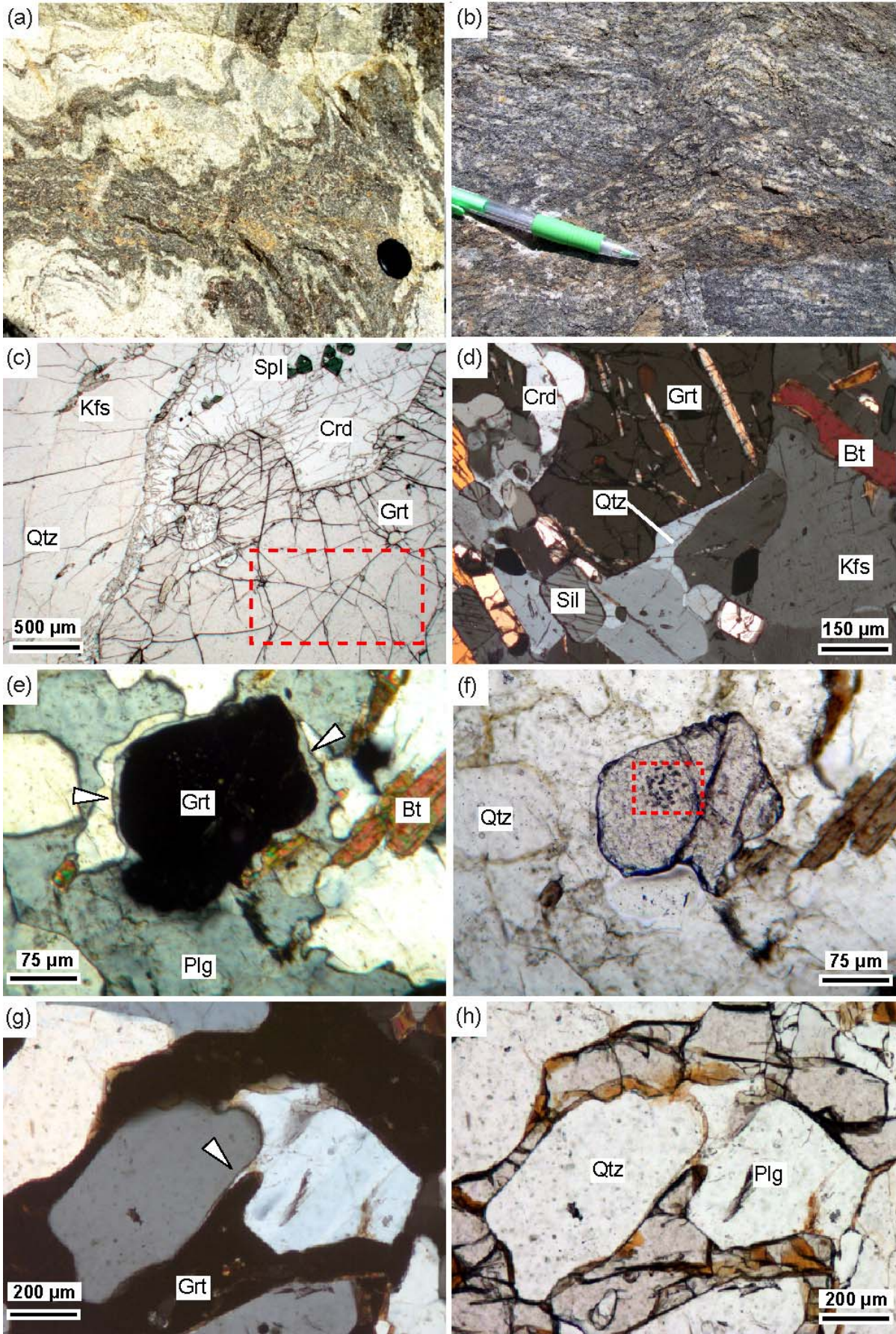


Fig.1

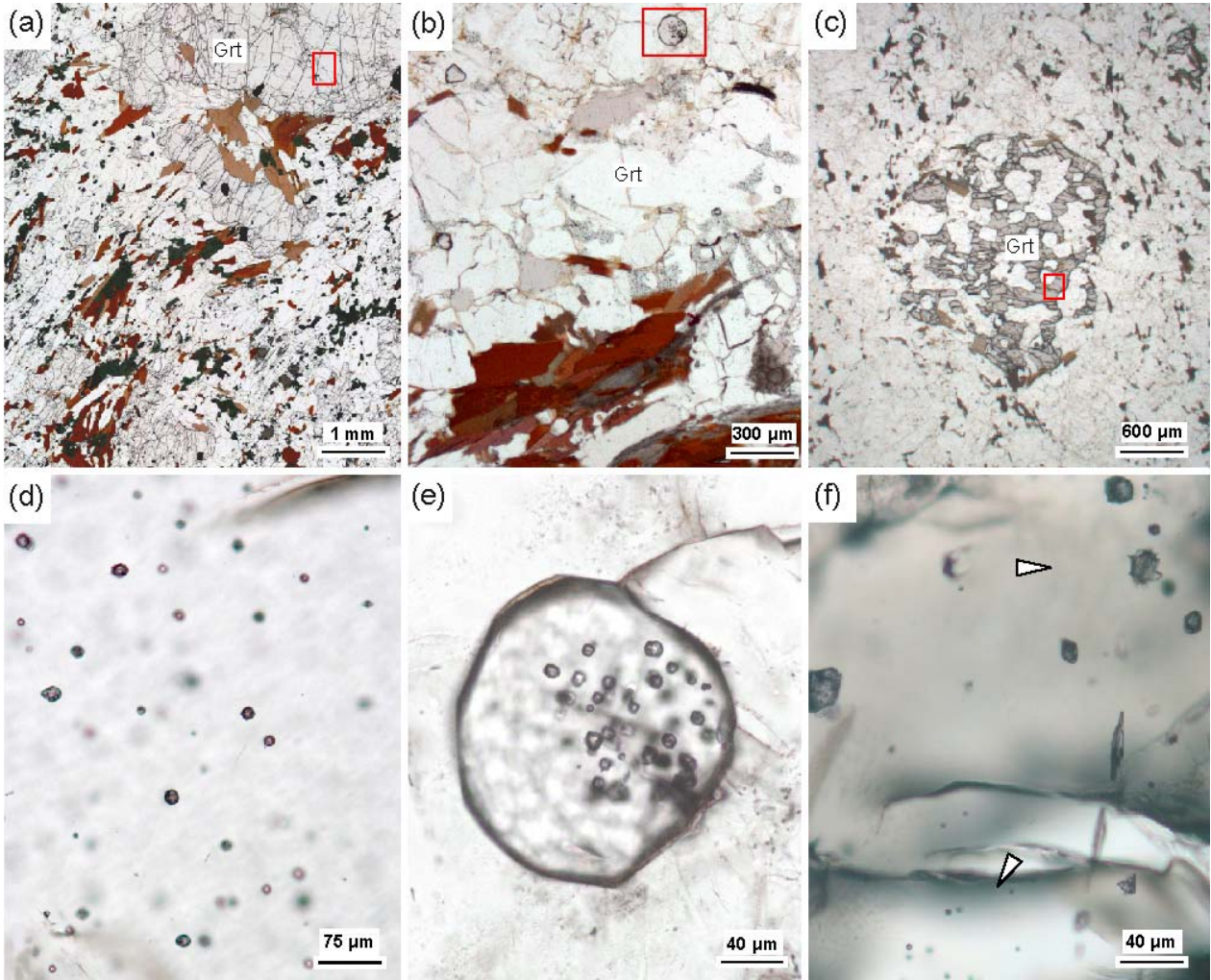


Fig.2

944
945
946

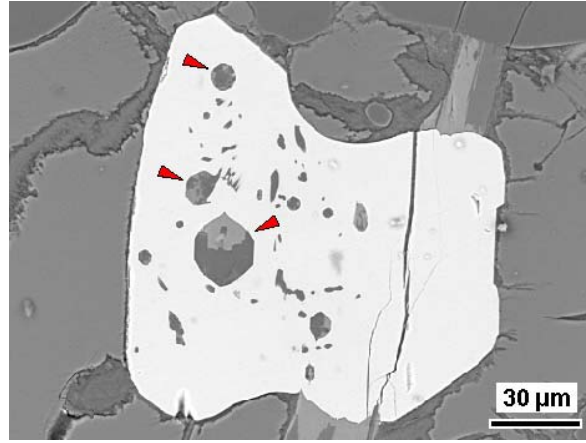


Fig.3

947
948

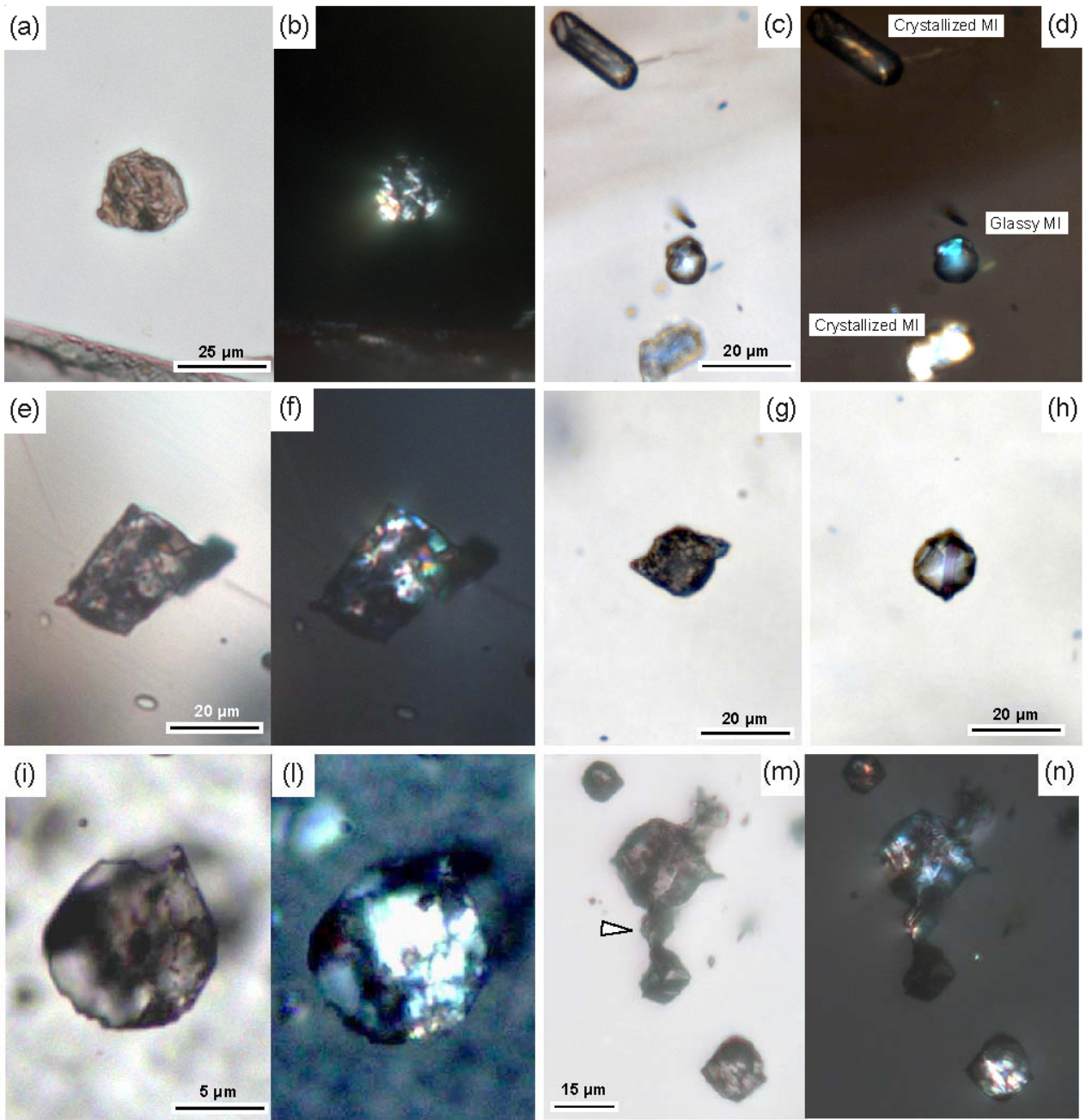


Fig.4

949
950
951

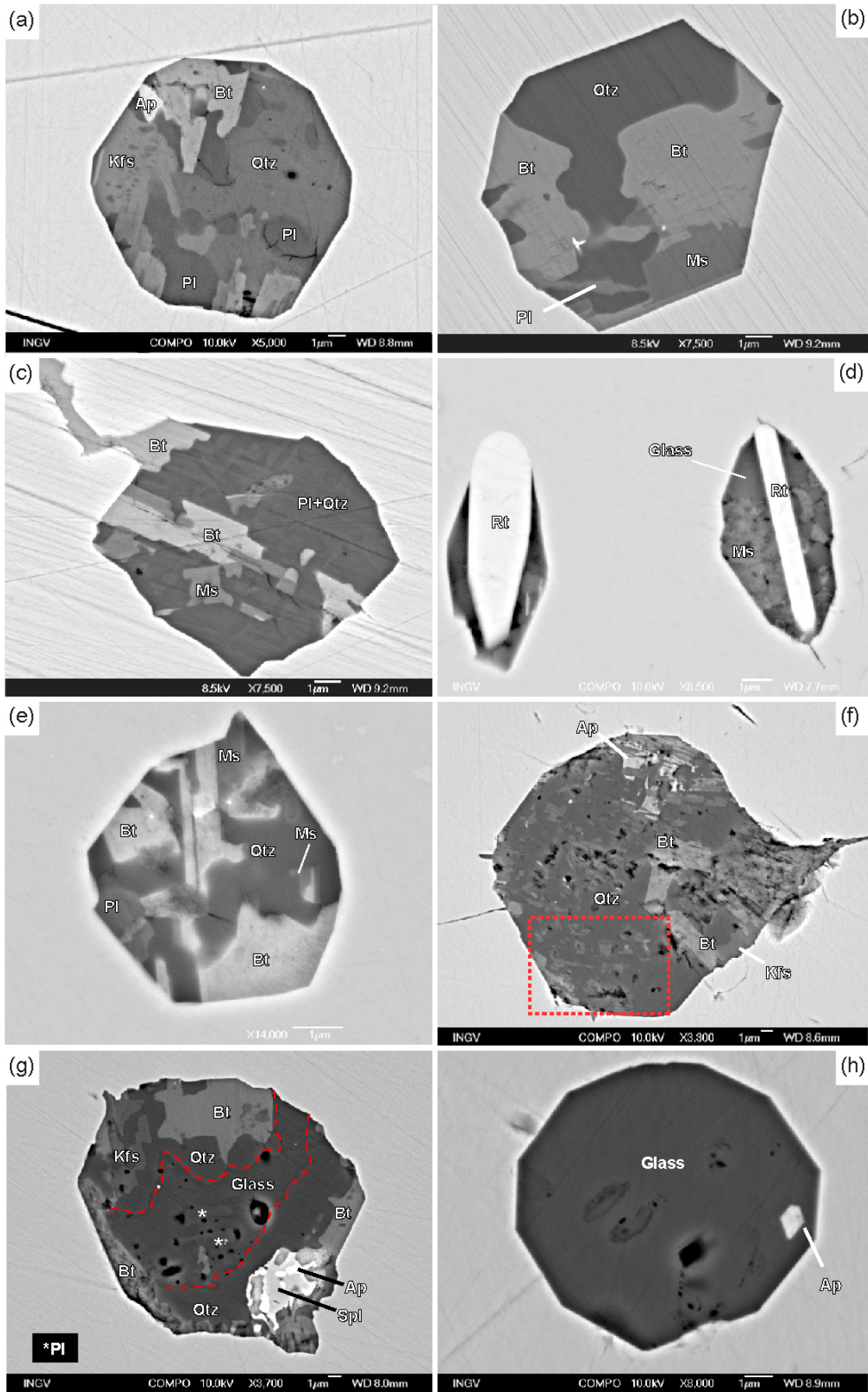
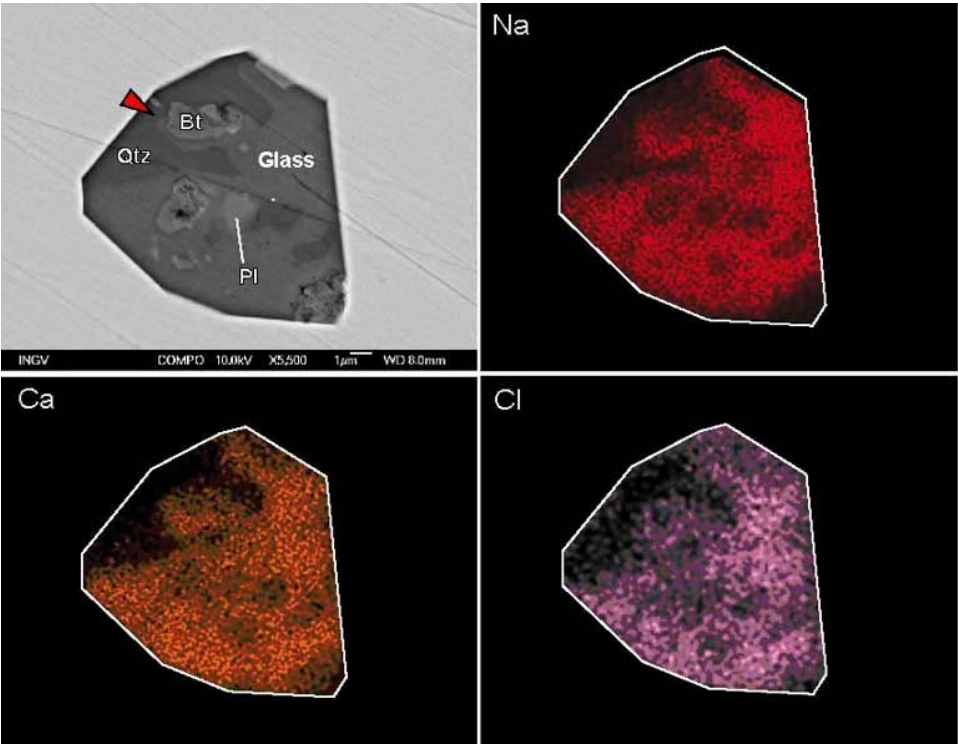


Fig5

954



955

956

957

Fig.7

958

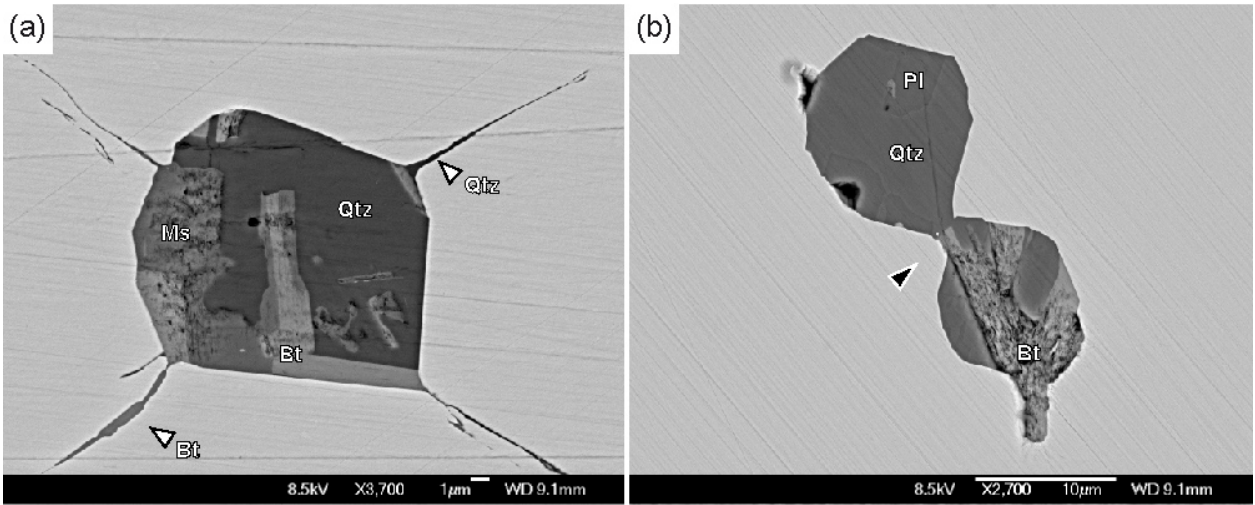


Fig.8

959

960

961

962

963

964

965

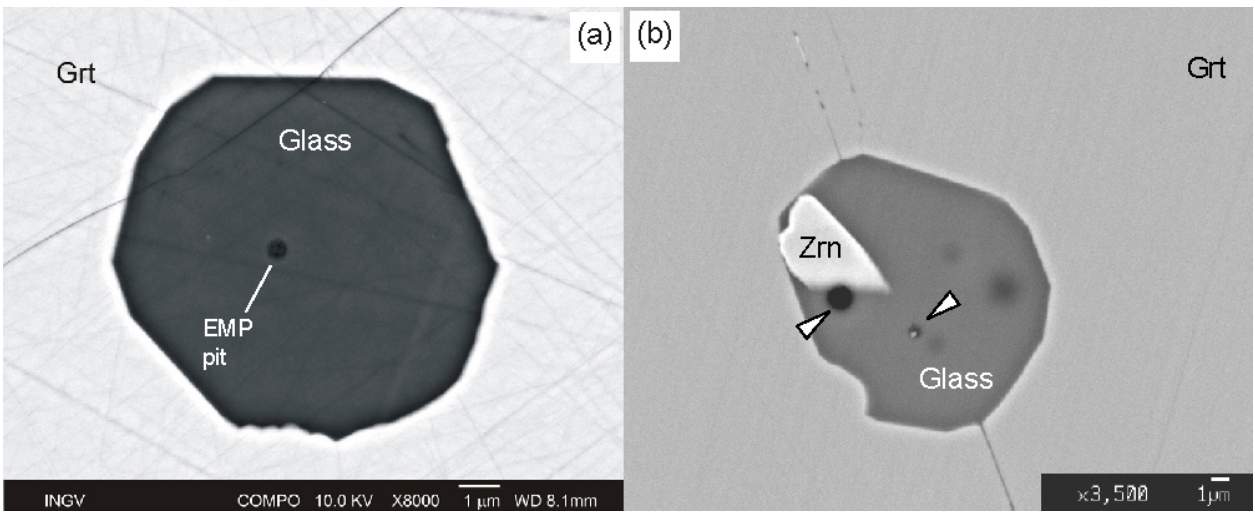
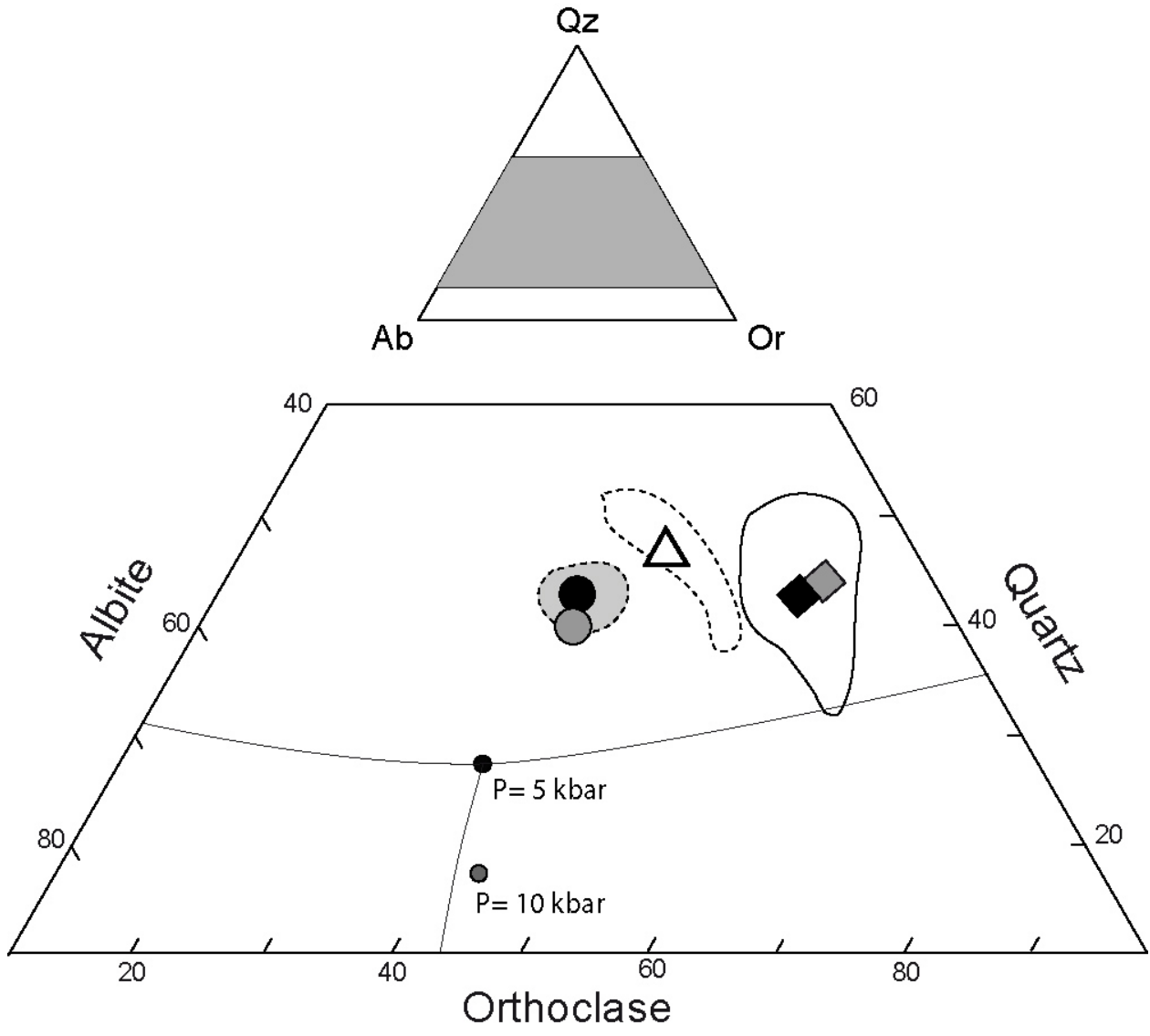


Fig. 9

966

967



●● Ronda metatexites

△ Barun gneisses

◆◆ Khondalites

Fig.10

968
969
970

Ronda migmatites

Barun gneisses

	<i>Homogenized MI</i>						<i>Glassy inclusions</i>				<i>Homogenized MI</i>				
	1	2	3	4	5	Aver.	13	1	6	Aver.	5_1	5_7	9_1	9_2	Aver.
SiO ₂	68,62	67,23	67,67	70,21	70,18	68,78	68,42	71,70	68,95	69,69	73,37	71,25	73,57	76,90	73,77
TiO ₂	0,26	0,00	0,00	0,15	0,01	0,08	0,00	0,00	0,24	0,08	0,21	0,02	0,07	0,08	0,09
Al ₂ O ₃	11,39	11,07	11,28	11,31	12,03	11,42	11,57	12,16	11,63	11,78	12,97	14,85	12,40	11,38	12,90
FeO	1,82	1,86	1,55	1,45	1,27	1,59	1,26	1,27	1,07	1,2	2,70	2,93	2,25	2,14	2,51
MnO	0,12	0,18	0,21	0,11	0,06	0,14	0,19	0,03	0,04	0,09	0,31	0,48	0,11	0,12	0,25
MgO	0,18	0,07	0,26	0,01	0,07	0,12	0,06	0,05	0,10	0,07	0,67	0,63	0,41	0,42	0,53
CaO	0,52	0,53	0,42	0,29	0,45	0,44	0,31	0,25	0,60	0,39	0,79	1,51	0,73	0,38	0,85
Na ₂ O	2,58	2,42	2,56	3,02	3,14	2,74	3,37	2,96	2,93	3,09	1,89	1,86	2,12	1,87	1,94
K ₂ O	4,18	4,31	3,72	3,75	4,05	4,00	4,05	4,07	4,45	4,19	4,47	5,71	3,97	5,30	4,86
P ₂ O ₅	0,11	0,76	0,63	0,00	0,22	0,35	0,04	0,00	0,49	0,18	0,04	0,04	0,00	0,00	0,02
Cl	n.a.	n.a.	n.a.	n.a.	n.a.	n.a.	n.a.	n.a.	n.a.	n.a.	n.a.	n.a.	n.a.	n.a.	n.a.
Total	89,78	88,45	88,30	90,28	91,48	89,66	89,27	92,48	90,50	90,76	97,42	99,27	95,64	98,59	97,73
Fluids by diff.	10,22	11,55	11,70	9,72	8,52	10,34	10,73	7,52	9,50	9,24	2,58	0,73	4,36	1,41	2,27
ASI	1,17	1,15	1,25	1,18	1,16	1,18	1,10	1,25	1,08	1,14	1,38	1,24	1,36	1,20	1,29
Fe+Mg*	0,028	0,030	0,031	0,020	0,020	0,026	0,022	0,019	0,015	0,019	0,056	0,063	0,042	0,041	0,050
CIPW normative minerals															
Cor	2	3	2	2	3	3	1	2	2	2	4	3	3	2	3
Qz	35	37	36	35	36	36	31	37	34	34	40	32	42	43	39
Ab	20	22	26	27	23	23	28	25	25	26	16	16	18	16	16
Or	25	22	22	24	24	24	24	24	26	25	26	34	23	31	29
An	0	0	1	1	0	0	1	1	0	1	4	7	4	2	4

72

73 **Table 1 (continua)**

74

Khondalites

	<i>Homogenized MI</i>											<i>Glassy inclusions</i>				
	12_1	12_8	10_7	9_1	9_2	7_5	7_6	6_1	6_3	4_5	4_11	Aver.	246	8_1	8_3	Aver.
SiO ₂	70,87	74,11	69,24	77,02	76,28	75,84	76,81	75,92	72,93	72,08	72,42	73,96	77,27	77,91	77,98	77,72
TiO ₂	0,00	0,27	0,18	0,00	0,10	0,02	0,11	0,20	0,11	0,18	0,00	0,11	0,00	0,13	0,00	0,04
Al ₂ O ₃	14,45	13,86	14,90	12,62	11,11	11,93	11,32	11,71	14,12	12,99	13,41	12,95	11,96	11,90	11,84	11,90
FeO	3,18	2,94	4,13	2,73	3,12	2,70	2,16	2,38	2,47	3,14	4,39	3,03	0,91	0,97	1,15	1,01
MnO	0,06	0,07	0,07	0,01	0,08	0,00	0,06	0,00	0,00	0,00	0,06	0,04	0,00	0,00	0,11	0,04
MgO	0,72	0,42	0,90	0,67	0,40	0,43	0,62	0,99	0,91	0,66	0,45	0,65	0,02	0,02	0,00	0,01
CaO	0,48	0,70	0,88	0,55	0,54	0,11	0,33	0,57	0,54	0,51	0,63	0,53	0,03	0,00	0,06	0,03
Na ₂ O	1,41	1,02	1,24	0,51	0,70	0,80	1,30	1,07	1,24	1,48	1,38	1,10	1,02	0,98	0,91	0,97
K ₂ O	8,19	7,04	6,24	6,66	6,36	7,14	6,24	5,83	7,60	6,23	6,43	6,72	7,56	7,27	7,96	7,60
P ₂ O ₅	0,04	0,10	0,00	0,02	0,02	0,17	0,00	0,00	0,00	0,02	0,02	0,03	n.a.	0,12	0,19	0,15
Cl	0,36	0,21	0,34	0,08	0,14	0,09	0,18	0,20	0,37	0,44	0,33	0,25	n.a.	n.a.	n.a.	n.a.
Total	99,76	100,74	98,12	100,86	98,85	99,23	99,12	98,88	100,29	97,73	99,53	99,37	98,77	99,29	100,21	99,47
Fluids by diff.	0,24	-0,74	1,88	-0,86	1,16	0,77	0,88	1,12	-0,29	2,27	0,47	0,63	1,23	0,71	-0,20	0,53
ASI	1,20	1,31	1,43	1,39	1,23	1,29	1,19	1,29	1,26	1,29	1,29	1,29	1,21	1,26	1,16	1,21
Fe+Mg*	0,063	0,049	0,078	0,055	0,053	0,048	0,045	0,055	0,056	0,058	0,073	0,056	0,013	0,012	0,018	0,014
CIPW normative minerals																
Cor	2	4	4	4	2	3	2	3	3	3	3	3	2	3	2	2
Qz	31	42	40	50	50	46	47	50	37	42	41	37	42	46	46	42
Ab	14	10	13	5	7	7	12	11	12	15	14	9	9	7	9	8
Or	56	48	47	45	43	47	41	40	51	44	45	40	45	47	45	45
An	2	3	4	3	3	0	2	3	3	2	3	2	0	0	0	0

75
76

	Ronda migmatites										Barun gneisses					Khondalites																
	Homogenized MI					Glassy inclusions					Homogenized MI					Homogenized MI						Glassy inclusions										
	1	2	3	4	5	Aver.	13	1	6	Aver.	5_1	5_7	9_1	9_2	Aver.	12_1	12_8	10_7	9_1	9_2	7_5	7_6	6_1	6_3	4_5	4_11	Aver.	246	8_1	8_3	Aver.	
SiO ₂	68,62	67,23	67,67	70,21	70,18	68,78	68,42	71,70	68,95	69,69	73,37	71,25	73,57	76,90	73,77	70,87	74,11	69,24	77,02	76,28	75,84	76,81	75,92	72,93	72,08	72,42	73,96	77,27	77,91	77,98	77,72	
TiO ₂	0,26	0,00	0,00	0,15	0,01	0,08	0,00	0,00	0,24	0,08	0,21	0,02	0,07	0,08	0,09	0,00	0,27	0,18	0,00	0,10	0,02	0,11	0,20	0,11	0,18	0,00	0,11	0,00	0,13	0,00	0,04	
Al ₂ O ₃	11,39	11,07	11,28	11,31	12,03	11,42	11,57	12,16	11,63	11,78	12,97	14,85	12,40	11,38	12,90	14,45	13,86	14,90	12,62	11,11	11,93	11,32	11,71	14,12	12,99	13,41	12,95	11,96	11,90	11,84	11,90	
FeO	1,82	1,86	1,55	1,45	1,27	1,59	1,26	1,27	1,07	1,2	2,70	2,93	2,25	2,14	2,51	3,18	2,94	4,13	2,73	3,12	2,70	2,16	2,38	2,47	3,14	4,39	3,03	0,91	0,97	1,15	1,01	
MnO	0,12	0,18	0,21	0,11	0,06	0,14	0,19	0,03	0,04	0,09	0,31	0,48	0,11	0,12	0,25	0,06	0,07	0,07	0,01	0,08	0,00	0,06	0,00	0,00	0,00	0,06	0,04	0,00	0,00	0,11	0,04	
MgO	0,18	0,07	0,26	0,01	0,07	0,12	0,06	0,05	0,10	0,07	0,67	0,63	0,41	0,42	0,53	0,72	0,42	0,90	0,67	0,40	0,43	0,62	0,99	0,91	0,66	0,45	0,65	0,02	0,02	0,00	0,01	
CaO	0,52	0,53	0,42	0,29	0,45	0,44	0,31	0,25	0,60	0,39	0,79	1,51	0,73	0,38	0,85	0,48	0,70	0,88	0,55	0,54	0,11	0,33	0,57	0,54	0,51	0,63	0,53	0,03	0,00	0,06	0,03	
Na ₂ O	2,58	2,42	2,56	3,02	3,14	2,74	3,37	2,96	2,93	3,09	1,89	1,86	2,12	1,87	1,94	1,41	1,02	1,24	0,51	0,70	0,80	1,30	1,07	1,24	1,48	1,38	1,10	1,02	0,98	0,91	0,97	
K ₂ O	4,18	4,31	3,72	3,75	4,05	4,00	4,05	4,07	4,45	4,19	4,47	5,71	3,97	5,30	4,86	8,19	7,04	6,24	6,66	6,36	7,14	6,24	5,83	7,60	6,23	6,43	6,72	7,56	7,27	7,96	7,60	
P ₂ O ₅	0,11	0,76	0,63	0,00	0,22	0,35	0,04	0,00	0,49	0,18	0,04	0,04	0,00	0,00	0,02	0,04	0,10	0,00	0,02	0,02	0,17	0,00	0,00	0,00	0,02	0,02	0,03	n.a.	0,12	0,19	0,15	
Cl	n.a.	n.a.	n.a.	n.a.	n.a.	n.a.	n.a.	n.a.	n.a.	n.a.	n.a.	n.a.	n.a.	n.a.	n.a.	0,36	0,21	0,34	0,08	0,14	0,09	0,18	0,20	0,37	0,44	0,33	0,25	n.a.	n.a.	n.a.	n.a.	
Total	89,78	88,45	88,30	90,28	91,48	89,66	89,27	92,48	90,50	90,76	97,42	99,27	95,64	98,59	97,73	99,76	100,74	98,12	100,86	98,85	99,23	99,12	98,88	100,29	97,73	99,53	99,37	98,77	99,29	100,21	99,47	
Fluids by diff.	10,22	11,55	11,70	9,72	8,52	10,34	10,73	7,52	9,50	9,24	2,58	0,73	4,36	1,41	2,27	0,24	-0,74	1,88	-0,86	1,16	0,77	0,88	1,12	-0,29	2,27	0,47	0,63	1,23	0,71	-0,20	0,53	
ASI	1,17	1,15	1,25	1,18	1,16	1,18	1,10	1,25	1,08	1,14	1,38	1,24	1,36	1,20	1,29	1,20	1,31	1,43	1,39	1,23	1,29	1,19	1,29	1,26	1,29	1,29	1,29	1,21	1,26	1,16	1,21	
Fe+Mg*	0,028	0,030	0,031	0,020	0,020	0,026	0,022	0,019	0,015	0,019	0,056	0,063	0,042	0,041	0,050	0,063	0,049	0,078	0,055	0,053	0,048	0,045	0,055	0,056	0,058	0,073	0,056	0,013	0,012	0,018	0,014	
CIPW normative minerals																																
Cor	2	3	2	2	3	3	1	2	2	2	4	3	3	2	3	2	4	4	4	2	3	2	3	3	3	3	3	2	3	2	2	
Qz	35	37	36	35	36	36	31	37	34	34	40	32	42	43	39	31	42	40	50	50	46	47	50	37	42	41	37	42	46	46	42	
Ab	20	22	26	27	23	23	28	25	25	26	16	16	18	16	16	14	10	13	5	7	7	12	11	12	15	14	9	9	7	9	8	
Or	25	22	22	24	24	24	24	24	26	25	26	34	23	31	29	56	48	47	45	43	47	41	40	51	44	45	40	45	47	45	45	
An	0	0	1	1	0	0	1	1	0	1	4	7	4	2	4	2	3	4	3	3	0	2	3	3	2	3	2	0	0	0	0	

77
78